Geophysical Journal International

Geophys. J. Int. (2020) **223,** 111–131
Advance Access publication 2020 June 20
GJI Geodynamics and Tectonics

doi: 10.1093/gji/ggaa299

The role of crustal models in the dynamics of the India–Eurasia collision zone

Srishti Singh and Attreyee Ghosh

Centre for Earth Sciences, Indian Institute of Science, Bangalore 560012*, India. E-mail:* srishtis@iisc.ac.in

Accepted 2020 June 12. Received 2020 May 19; in original form 2020 January 16

SUMMARY

We investigate how different crustal models can affect the stress field, velocities and associated deformation in the India–Eurasia collision zone. We calculate deviatoric stresses, which act as deformation indicators, from topographic load distribution and crustal heterogeneities coupled with density driven mantle convection constrained by tomography models. We use three different crustal models, CRUST2.0, CRUST1.0 and LITHO1.0 and observe that these models have different crustal thickness and densities. As a result, gravitational potential energy (GPE) calculated based on these densities and crustal thicknesses differ between these models and so do the associated deviatoric stresses. For GPE only models, LITHO1.0 provides a better constraint on deformation as it yields the least misfit (both orientation and relative magnitude) with the surface observations of strain rates, lithospheric stress, plate motions and earthquake moment tensors. However, when the stresses from GPE are added to those associated with mantle tractions arising from density-driven mantle convection, the coupled models in all cases provide a better fit to surface observations. The N–S tensional stresses predicted by CRUST2.0 in this area get reduced significantly due to addition of large N–S compressional stresses predicted by the tomography models S40RTS and SAW642AN leading to an overall strike-slip regime. On the other hand, the hybrid models, SINGH_S40RTS and SINGH_SAW that are obtained by embedding a regional *P*-wave model, Singh *et al.*, in global models of S40RTS and SAW642AN, predict much lower compression within this area. These hybrid models provide a better constraint on surface observations when coupled with CRUST1.0 in central Tibet, whereas the combined LITHO1.0 plus mantle traction model provides a better fit in some other areas, but with a degradation of fit in central Tibet.

Key words: Numerical modelling; Crustal structure; Dynamics:gravity and tectonics; Dynamics of lithosphere and mantle; Kinematics of crustal and mantle deformation.

1 INTRODUCTION

The India–Eurasia (IN–EU) collision zone was formed when the Indian and Eurasian plates collided ∼50–70 Ma, leading to the formation of the highest mountains on Earth (Molnar & Tapponnier 1975). The area exhibits a complex deformation pattern, with different styles of deformation, localized and confined in different regions (Molnar *et al.* 1993). Various studies (England & McKenzie 1982; Flesch *et al.* 2001; Ghosh *et al.* 2006; Bischoff & Flesch 2018a, b; Singh & Ghosh 2019; Capitanio 2020) have attempted to understand the forces behind deformation of this region using numerical models of lithosphere and/or mantle dynamics. However, there is still no agreement on the relative contribution of different forces causing deformation in this area. The forces behind deformation arise due to two primary sources: (i) topography and lateral density variations within the lithosphere and (ii) tractions acting at the base of the lithosphere originating from density-driven mantle convection. The forces associated with topography and density variations within the lithosphere can be estimated by computing gradients of gravitational potential energy (GPE) that give rise to deviatoric stresses.

Various studies have calculated these GPE related deviatoric stresses either by using simple analytical models (Artyushkov 1973; Molnar & Lyon-Caen 1988; Schmalholz *et al.* 2014), or by using thin viscous sheet (TVS) models (England & McKenzie 1982, 1983; England & Houseman 1986; Houseman & England 1986; England & Molnar 1997; Flesch *et al.* 2001; Ghosh *et al.* 2006, 2009; Stamps *et al.* 2014; Finzel *et al.* 2015; Hirschberg *et al.* 2018). In TVS models, the lithosphere is treated as a homogeneous continuous sheet with or without lateral strength variations. In these models, the gradient of shear tractions is assumed to be negligible as compared to the buoyancy forces acting on density. The dynamics of the IN–EU collision zone has been studied by using TVS models to constrain the deviatoric stresses arising due to GPE differences (England & Houseman 1989; Flesch *et al.* 2001; Ghosh *et al.* 2006; Singh & Ghosh 2019). England & Houseman (1986, 1988) predicted the basic feature of continental deformation in Tibet and surrounding areas using a TVS model, however, they were unable to reproduce the large scale E–W extension in this area. Flesch *et al.* (2001) used a similar TVS approximation, but with a uniformly viscous lithosphere to compute vertically averaged deviatoric stress within the lithosphere. Ghosh *et al.* (2006) used a similar approach but with lateral viscosity variations within the lithosphere and showed that GPE related stresses computed from the CRUST2.0 model overpredict N–S extension in the Tibetan plateau. Jay *et al.* (2017) studied the deformation and force balance in the Pamir plateau using standard TVS approximation. They concluded that stresses causing deformation and driving plate motion in this area result from GPE variations and the IN–EU convergence, accommodated at the Pamir frontal trust. Liu & Yang (2003) used a 3-D viscoelastic model to explore the relative contributions of GPE, rheological structure, basal shear and boundary conditions in the crustal extension of the Tibetan plateau. Bischoff & Flesch (2018a) computed the dynamic response of this region (3-D velocity and deviatoric stress) by using a 3-D finite element (FE) model of the IN–EU collision zone and compared it to present-day GPS data. They also provided constraints on absolute values of 3-D viscosity in the upper crustal and mantle layers, and concluded that a laterally variable upper crust, with its strength decreasing from west to east, provided the best fit to surface motion in this region. Bischoff & Flesch (2018b) also performed 3-D lithospheric-scale simulations to investigate the lithospheric surface response of the IN–EU collision zone for a range of lower crustal viscosities.

In Singh & Ghosh (2019), we explained the deformation of the Indian Plate and the IN–EU collision zone by using a FE model based on TVS approximation. We computed GPE using the thickness and density of crustal layers derived from CRUST1.0 (Laske *et al.* 2013) model. The vertically averaged deviatoric stresses associated with GPE were computed by using the FE model (Flesch *et al.* 2001) up to 100 km depth by incorporating lateral viscosity variations within the lithosphere. To estimate the deviatoric stresses associated with deeper buoyancies, we used horizontal tractions, calculated from mantle flow models, acting at the base of the lithosphere thin sheet model. We tested various mantle flow models where densities were derived from a range of tomography models for two radially varying viscosity structures obtained from Ghosh *et al.* (2013b) and Steinberger & Holme (2008). The stresses associated with basal tractions derived from mantle flow were then added to those associated with GPE variations to compute the total stress field. We also calculated plate velocities, strain rates, as well as the most compressive horizontal principal stress (SH_{max}) axes and compared them with observations. We obtained the coupled model of GPE and tractions derived from SINGH_S40RTS tomography model, as the best model, which provided the least misfits with various observational constraints for the entire study region. The tomography model, SINGH_S40RTS resulted from embedding the local tomography model of Singh *et al.* (2014) in the global model of S40RTS (Ritsema *et al.* 2011). However, we observed significant misfits in velocities, especially to GPS velocity vectors in the IN–EU collision zone for this model, particularly in the eastern Himalayan syntaxis (EHS, see fig. 12 of Singh & Ghosh (2019)). Also, the correlation of deviatoric stresses with observed strain rates was observed to degrade near the Pamir and the eastern part of the Tibetan plateau (see fig. 9 of Singh & Ghosh 2019). The combined model of GPE and tractions derived from SAW642AN tomography model (Mégnin & Romanowicz 2000), though did not give the lowest total error, performed slightly better in predicting stresses and velocities in the IN–EU collision zone (figs 9 AND 12 of Singh & Ghosh 2019).

In this paper, we primarily focus on the IN–EU collision zone to investigate possible reasons behind the misfits between the predicted and observed parameters. Whether the reasons for such misfits lie with uncertainty in the crustal models or with the inability of mantle flow models to properly constrain basal tractions in this region, due to inaccuracies in tomography models, is not clear. Hence, we test three crustal and lithospheric models, CRUST1.0, CRUST2.0 (Laske *et al.* 2001) and LITHO1.0 (Pasyanos *et al.* 2014) for calculating GPE, to verify whether uncertainty in thickness and density of crustal layers contribute to the observed misfits. The vertically averaged deviatoric stresses associated with GPE are then computed using the FE model (Flesch *et al.* 2001) up to 100 km depth for a lithosphere that is laterally varying in strength. In order to calculate the stresses associated with mantle tractions, we use a mantle convection model, HC (Hager & O'Connell 1981; Milner *et al.* 2009) driven by density anomalies derived from tomography models. Wang *et al.* (2015, 2019) and Singh & Ghosh (2019) showed that S40RTS and SAW642AN models provided a good fit to surface observables using joint modeling of lithosphere and mantle dynamics approach. Hence, we also use S40RTS and SAW642AN tomography models along with their hybrid counterparts, SINGH_S40RTS and SINGH_SAW, which are obtained by embedding the Singh *et al.* (2014) tomography model in these global models, respectively. The mantle tractions are computed from these four models for two radially varying viscosity structures, GHW13 (Ghosh *et al.* 2013b) and SH08 (Steinberger & Holme 2008) that had shown good match to surface observations (Wang *et al.* 2019). The stresses associated with these tractions are then added to those obtained from GPE only models, to account for both the sources of deformation in this region.

2 METHOD

2.1 Contribution from topography and density variations within the lithosphere

The stress field associated with both the sources of deformation, GPE as well as mantle tractions, are obtained by solving the force balance equation:

$$\frac{\partial \sigma_{ij}}{\partial x_j} + \rho g_i = 0, \tag{1}$$

where σ_{ij} is the ijth component of the total stress tensor, x_j is the jth coordinate axis, ρ is the density and g_i is the acceleration due to gravity (England & Molnar 1997). We solve these equations in spherical coordinates as in Ghosh *et al.* (2013b) using the FE method of Flesch *et al.* (2001) (Ghosh *et al.* 2013b; Singh & Ghosh 2019).

The above eq. (1) is expanded in z-direction and integrated from surface to a uniform reference level L, taken as 100 km below sea level. Using the thin sheet approximation, which states that

$$\frac{\partial}{\partial x}\int_{-h}^{L} \sigma_{xz} \mathrm{d}z + \frac{\partial}{\partial y}\int_{-h}^{L} \sigma_{yz} \mathrm{d}z << -\int_{-h}^{L} \rho g_z \mathrm{d}z, \tag{2}$$

we obtain the vertical stress (σ_{zz}) as

$$\sigma_{zz} = -\int_{-h}^{z} \rho(z')g\mathrm{d}z'. \tag{3}$$

The total stress, σ_{ij}, in eq. (1) is substituted by the deviatoric stress, τ_{ij}, using the relationship, $\tau_{ij} = \sigma_{ij} - \frac{1}{3}\sigma_{kk}\delta_{ij}$, where δ_{ij} is the Kronecker delta and $\frac{1}{3}\sigma_{kk}$ is the mean stress. The resultant full horizontal force balance equations can be written as

$$\frac{\partial \overline{\tau}_{xx}}{\partial x} - \frac{\partial \overline{\tau}_{zz}}{\partial x} + \frac{\partial \overline{\tau}_{xy}}{\partial y} = -\frac{\partial \overline{\sigma}_{zz}}{\partial x} + \tau_{xz}(L) \tag{4}$$

$$\frac{\partial \overline{\tau}_{yx}}{\partial x} + \frac{\partial \overline{\tau}_{yy}}{\partial y} - \frac{\partial \overline{\tau}_{zz}}{\partial y} = -\frac{\partial \overline{\sigma}_{zz}}{\partial y} + \tau_{yz}(L), \tag{5}$$

where the over bars represent depth integration. The first terms on the right-hand side of eqs (4) and (5) represent horizontal gradients in GPE per unit area, whereas $\tau_{xz}(L)$ and $\tau_{yz}(L)$ represent the tractions at the base of the thin sheet (lithosphere) at depth L, arising from density driven mantle convection (Ghosh *et al.* 2009).

In order to calculate the stresses associated with GPE variations, we use crustal thickness as well as density data from three crustal models: CRUST2.0, CRUST1.0 and LITHO1.0. CRUST2.0 is an updated $2^\circ \times 2^\circ$ version of CRUST5.1 (Mooney *et al.* 1998), which is a global model for crustal thickness and density based on seismic data and a detailed compilation of ice and sediment thickness. Similarly, CRUST1.0 model provides 1° averages of crustal thickness as well as density data that are obtained from active source seismic studies as well as from receiver function studies. LITHO1.0 is a 1° tessellated model of the crust and uppermost mantle that was created by perturbing the starting model (CRUST1.0) to fit high-resolution surface wave dispersion data. We compare the thickness and density distribution of crustal layers for these three models and find that they differ from each other considerably in the region of interest (Fig. 1). The upper crustal thickness is largest for CRUST1 model ($\sim$35 km), while it is lowest for LITHO model ($\sim$20 km). The middle crustal layer is observed to have similar thickness for CRUST2 and LITHO models (>22 km), although it is somewhat higher for CRUST2 (Figs 1d and f). The lower crustal layer is thickest for LITHO model (>30 km, Fig. 1i), while CRUST1 contains the thinnest lower crust (<20 km, Fig. 1h). LITHO model is observed to have much lower density for all crustal layers compared to the other two crustal models (Fig. 1, bottom three panels). The densities of the middle and lower crust in CRUST2 are observed to be the highest among all the models (Figs 1m and p), while the upper crust of CRUST1 has the highest density (Fig. 1k). As for the density of lithospheric mantle, we use a constant density of 3300 kg m^{-3} for all three models.

We use the densities and crustal thickness from the abovementioned crustal and lithospheric models to compute the vertically integrated vertical stress, $\overline{\sigma}_{zz}$, integrated from the top of variable topography up to a common reference depth (England & Molnar 1997; Flesch *et al.* 2001; Ghosh *et al.* 2006, 2009), which is given by negative of GPE per unit area :

$$\overline{\sigma}_{zz} = -\int_{-h}^{L}\left[\int_{-h}^{z} \rho g(z')\mathrm{d}z'\right] = -\int_{-h}^{L}(L-z)\rho(z)g\mathrm{d}z. \tag{6}$$

Here, $\rho(z)$ is the density, L is the depth to the base of the thin sheet, which is taken as 100 km, h is the topographic elevation, z' is a variable of integration and g is the acceleration due to gravity. Using the GPE differences and setting the traction terms to zero in the force balance equation, the solution to eq. (1) is obtained by applying a FE technique on a global grid of $1^\circ \times 1^\circ$ [Flesch *et al.* 2001, for detailed methodology, refer to Ghosh *et al.* (2013b) and Singh & Ghosh (2019)]. We also incorporate lateral strength variations in the lithospheric FE model by taking into account weak plate boundaries, cratons and age of oceanic plates so that there is about an order of magnitude difference between the old and young ocean floors (Fig. S1a). Since this lateral viscosity structure still produced large misfits with observational constraints within the IN–EU collision zone in Singh & Ghosh (2019), we make some minor modification to this viscosity structure. We assign the area around Shillong plateau the same viscosity as the intraplate region ($\sim 10^{23}$ Pa-s, Fig. S1b). The reason behind this is that although earthquakes have been reported from the Shillong plateau area, several studies have ascribed this region as a rigid 'pop-up' structure bounded by faults (Bilham & England 2001; Islam *et al.* 2011).

The above models are uncompensated, i.e. they have variable pressure at the base of the lithosphere. These uncompensated models also include the effect of radial tractions acting at the base of the lithosphere from deeper mantle density buoyancies (i.e. dynamic topography) in addition to lithospheric buoyancies (see Ghosh *et al.* 2013b). To investigate the consequences of excluding these radial tractions, in some cases we compensate these crustal models by assuming a uniform pressure at the base of the lithosphere ($\sim$100 km below sea level). This uniform pressure is calculated by taking the average pressure at the reference level (*cf.* Ghosh *et al.* 2009). In accordance with the Pratt (1855) model of isostasy that is based on constant thickness crustal blocks of variable density, we obtain isostatic equilibrium at 100 km depth by adjusting the density of the upper mantle layer. The adjusted densities of lithospheric mantle for all three models are shown in Fig. S2. As the LITHO1.0 model has the lowest density for crustal layers in this region, thus leading to low crustal pressure, we obtain the highest compensated density of lithospheric mantle for this model (Fig. S2c). We use these compensated densities to compute GPE and associated deviatoric stresses.

In addition to deviatoric stresses, we also compute strain rates and plate velocities. The magnitudes of both strain rates and plate velocities are controlled by absolute values of viscosity. Hence, in a post-processing step (see Singh & Ghosh 2019), we calculate the scaling factor for the viscosity field that gives the minimum misfit between the dynamic (predicted) velocity field and the kinematic velocity field of Kreemer *et al.* (2014) in a no-net-rotation (NNR) frame.

2.2 Contribution from mantle convection

In order to compute the stresses associated with density driven mantle convection, we first need to obtain the horizontal tractions acting at the base of the lithosphere. We use a semi-analytical, spherical mantle flow code, HC (Hager & O'Connell 1981; Milner *et al.* 2009), where flow is driven by density anomalies derived from seismic tomography models to compute these basal tractions. The required input parameters in HC are: mantle density anomalies, radial viscosity structure and seismic velocity–density scaling ($\mathrm{dln}_\rho/\mathrm{dln}v$). The density anomalies are derived from two global tomography models, S40RTS and SAW642AN along with two hybrid tomography models: SINGH_S40RTS and SINGH_SAW using a velocity–density scaling of 0.25 for *S*-wave models and 0.5 for *P*-wave models (*cf.* Ghosh *et al.* 2017). The hybrid models are obtained by embedding the regional tomography model of Singh *et al.* (2014), within the global models of S40RTS and SAW642AN. The velocity anomalies in regional and global tomography models are rescaled to obtain comparable amplitudes and a smoothing filter is applied at

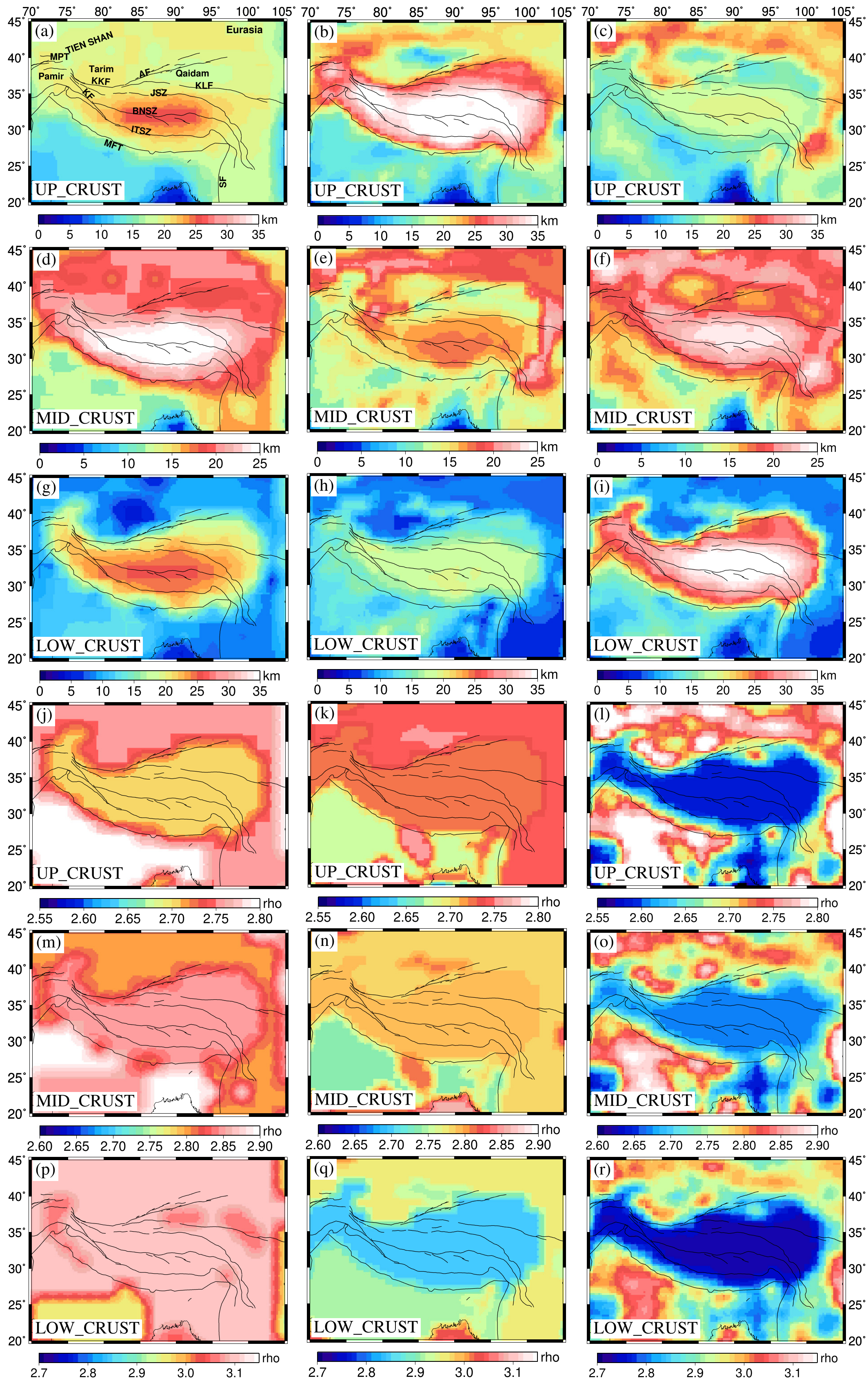

Figure 1. Comparison of thickness (top three rows) and density (bottom three rows) of crustal layers from CRUST2.0 (left-hand column), CRUST1.0 (middle column) and LITHO1.0 (right-hand column) models. MPT: Main Pamir Thrust; KF: Karakorum Fault; KKF: Karakax Fault; AF: Altyn Tagh fault; MFT: Main Frontal Thrust; ITSZ: Indus-Tsangpo Suture Zone; BNSZ: Bangong-Nujiang Suture Zone; JSSZ: Jinshajiang Suture Zone; KLF: Kunlun Fault; SF: Sagaing Fault.

the boundaries of merged/hybrid models to avoid any sudden jumps. We use two radially varying viscosity structures, GHW13 which is the best model of Ghosh *et al.* (2013b) and SH08 (Steinberger & Holme 2008), to compute horizontal tractions at ∼100 km depth. These tractions, like GPE, are taken as body force equivalents in the force balance equation (eq. 1). The body force distribution controls the direction and magnitude of deviatoric stresses within the lithosphere. HC does not include lateral viscosity variations, which are incorporated in our lithospheric FE model. The deviatoric stresses, thus computed from the tractions, are then added to those from GPE only models.

3 SURFACE OBSERVATIONS USED AS CONSTRAINTS

We use the strain rates from Global Strain Rate Model (GSRM v.2.1, Kreemer *et al.* 2014), $SH_{\max}$ (most compressive horizontal principal axes) stresses from the World Stress Map (WSM, Heidbach *et al.* 2018) and plate velocities from Kreemer *et al.* (2014) as constraints to evaluate the predicted deviatoric stresses in our study area (Fig. 2). We also use moment tensors from the global Centroid–Moment–Tensor (CMT) catalogue (Dziewonski *et al.* 1981; Ekström *et al.* 2012) as an additional constraint.

We compare our predicted deviatoric stresses with the GSRM strain rates (Fig. 2a) by computing a correlation coefficient using the following equation (Flesch *et al.* 2007; Ghosh *et al.* 2008; Singh & Ghosh 2019)

$$-1 \leq \sum_{areas}(\epsilon.\tau)\Delta S/\left(\sqrt{\sum_{areas}(E^2)\Delta S} * \sqrt{\sum_{areas}(T^2)\Delta S}\right) \leq 1, \quad (7)$$

where $E = \sqrt{\dot{\epsilon}_{\phi\phi}^2 + \dot{\epsilon}_{\theta\theta}^2 + \dot{\epsilon}_{rr}^2 + \dot{\epsilon}_{\phi\theta}^2 + \dot{\epsilon}_{\theta\phi}^2} = \sqrt{2\dot{\epsilon}_{\phi\phi}^2 + 2\dot{\epsilon}_{\phi\phi}\dot{\epsilon}_{\theta\theta} + 2\dot{\epsilon}_{\theta\theta}^2 + 2\dot{\epsilon}_{\phi\theta}^2}$, $T = \sqrt{\tau_{\phi\phi}^2 + \tau_{\theta\theta}^2 + \tau_{rr}^2 + \tau_{\phi\theta}^2 + \tau_{\theta\phi}^2} = \sqrt{2\tau_{\phi\phi}^2 + 2\tau_{\phi\phi}\tau_{\theta\theta} + 2\tau_{\theta\theta}^2 + 2\tau_{\phi\theta}^2}$, and $\epsilon.\tau = 2\dot{\epsilon}_{\phi\phi}\tau_{\phi\phi} + \dot{\epsilon}_{\phi\phi}\tau_{\theta\theta} + \dot{\epsilon}_{\theta\theta}\tau_{\phi\phi} + 2\dot{\epsilon}_{\theta\theta}\tau_{\theta\theta} + 2\dot{\epsilon}_{\phi\theta}\tau_{\phi\theta}$. Here E and T are second invariants of the strain rate and stress tensors, $\dot{\epsilon}_{ij}$ are the strain rates from GSRM, ΔS is the area, and τ_{ij} are the predicted deviatoric stresses.

We perform a quantitative comparison between our predicted $SH_{\max}$ axes and observed $SH_{\max}$ from WSM (Fig. 2b) by computing a total misfit (ϵ_p, Ghosh *et al.* 2013a; Singh & Ghosh 2019), given by $sin\theta(1 + R)$. Here, R is the regime misfit between the observed and predicted $SH_{\max}$, and θ is the angular deviation between the observed and predicted $SH_{\max}$ axes. R is calculated by assigning values between 1 and 3 to the $SH_{\max}$ stresses based on whether they are tensional, strike-slip or compressional. Hence, the difference in regime misfit (R) ranges from 0 to 2. The total misfit (ϵ_p) is a joint evaluation of both the angular and regime misfit and falls between 0 and 3.

In addition, we use the plate velocities from Kreemer *et al.* (2014) in a NNR frame, based on GPS observations, to constrain our models. We compute an RMS misfit (Ghosh & Holt 2012; Ghosh *et al.* 2013b) over the region of interest between the predicted and observed plate velocities. Moreover, we calculate the angular misfit between the predicted plate velocities and the observed velocities that yields values between 0° and 180°. Finally, we use the moment tensors from CMT and calculate the correlation as per eq. (7) where the $\dot{\epsilon}_{ij}$ are now the moment tensors. Since this constraint is found to be not as sensitive as the others, we only show the results using moment tensors in the Supporting Information (Fig. S3).

4 RESULTS

4.1 Predicting parameters using GPE contribution

The GPE computed in the IN–EU collision zone using eq. (6) is observed to be highest for CRUST2 model (Fig. 3a), while it is found to be very low for LITHO model (Fig. 3e). Such difference in GPE is due to the differences in the thickness and density distribution of these crustal models. As LITHO has much lower densities for all crustal layers (Fig. 1), it gives rise to low GPE in this area. On the other hand, CRUST2 is found to have the highest densities for most of the crustal layers, hence GPE for CRUST2 model is also observed to be the highest. The compensated model for CRUST2 is observed to have GPE similar to the uncompensated case (Fig. 3b). However, for CRUST1 and LITHO, the compensated cases yield slightly higher GPE (Figs 3d and f).

The predicted deviatoric stresses associated with GPE variations are also very different for the three different models. CRUST2 shows predominantly N–S oriented tensional stresses within the Tibetan Plateau with NW–SE orientation in south central Tibet (Figs 3a, b and 4a). CRUST1 also shows pure extension in Tibet although these tensional stresses are more E–W oriented, with the eastern and western parts showing a more N–S orientation (Figs 3c, d and 4b). The magnitudes of deviatoric stresses from CRUST1 within the plateau are also lower compared to those of CRUST2. When it comes to LITHO, the predicted stresses are different from both the other two crustal models. We see predominantly N–S to NE–SW oriented compression in the eastern and central parts of the plateau with E–W tension and strike-slip type of deformation in the western part (Figs 3e, f and 4c). The stresses within the Qaidam Basin and near EHS also show strike-slip pattern. South of the plateau, stresses are similar for the three models with NE–SW compression occurring in the Himalayas across MFT (Figs 3 and 4, top panel). The Tarim Basin also shows dominant compression for all three models. In the Pamir region, both CRUST2 and CRUST1 exhibit N–S to NE–SW tensional stresses as opposed to E–W tension and NW–SE compression predicted by LITHO [similar to the observed deformation in Pamir (Mohadjer *et al.* 2010; Jay *et al.* 2017)]. The compensated models are not very different from their uncompensated counterparts except for their slightly reduced amplitudes (Fig. 3, right-hand panel). Since the orientation of deviatoric stresses from the compensated models are very similar to those of the uncompensated cases and only differ in magnitudes, we restrict our subsequent discussion to the uncompensated models only as most of the observational constraints (except plate velocities) deal with the direction and style of deformation and not so much with the absolute magnitudes.

The total misfit between the observed (Fig. 2b) and predicted $SH_{\max}$ (Figs 4a–c) is shown in Figs 4(d)–(f). CRUST2 model shows a larger misfit (∼0.84) as compared to the other models, due to the dominant N–S tension in Tibet as opposed to the more E–W tension shown by the other models. The misfit in Tien-Shan and Tarim Basin for CRUST2 and CRUST1 (Figs 4d and e) gets reduced in LITHO (Fig. 4f). The region around Pamir also fares slightly better in LITHO. In fact, the entire western Tibet shows smaller misfit for LITHO compared to CRUST2 and CRUST1 models. In central Tibet, CRUST1 shows the lowest misfit. The compensated models show slightly higher total misfit for all three models (Table S1). We obtain the lowest total misfit for the uncompensated LITHO model with a regional average of 0.67 (Fig. 4f).

The correlation of deviatoric stress tensors with GSRM strain rate tensors is observed to have significant variation within Tibet (Figs 4g–i). CRUST1 shows a high correlation in central Tibet

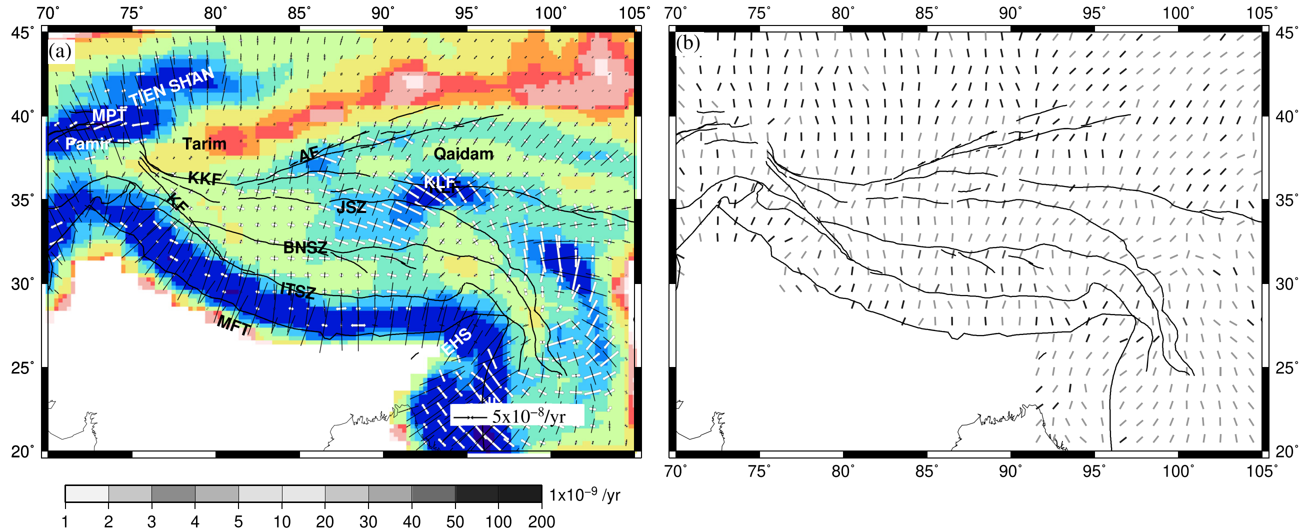

Figure 2. (a) GSRM strain rates obtained from Kreemer *et al.* (2014) plotted on top of second invariant of strain rate tensors. White denotes extensional whereas black denotes compressional strain. (b) Most compressive horizontal principal axes ($SH_{\max}$) from Heidbach *et al.* (2018), averaged within 1° × 1° areas. Red indicates normal fault regime, blue indicates thrust regime, whereas green denotes strike-slip regime.

(Fig. 4h), while an intermediate correlation (<0.5) is obtained for CRUST2 and LITHO models in that region, with the LITHO model faring slightly better (Figs 4g and i). This is mainly because the observed E–W tension in central Tibet is only predicted by CRUST1 whereas CRUST2 shows NW–SE tension and LITHO shows N–S compression (Fig. 3). The correlation is very poor in the Pamir, Tien Shan, the Karakorum (KF) and Karakax faults (KKF) as well as along the Indus-Tsangpo suture zone (ITSZ) for both CRUST2 and CRUST1 models. Most of these areas improve considerably in case of LITHO (Fig. 4i). A good correlation is observed along MFT for all the models, which suggests that all models are predicting the observed NE–SW compression along MFT. The correlation degrades after compensation for all the models (Fig. 12 and Table S1) due to the fact that compensated crustal models have a slightly higher GPE resulting in either an increment of N–S extension or a decrease of N–S compression (Fig. 3). The highest average correlation coefficient of 0.8 is obtained for the LITHO model (Fig. 4i).

We also compare our predicted deviatoric stress tensors from GPE variations with moment tensors (*cf.* Ghosh *et al.* 2019) by using eq. (7), where components of strain rate tensors are replaced by corresponding components of moment tensors. The moment tensors obtained from the Global CMT catalogue are smoothed on a 1° × 1° grid. As our models are found to be fairly insensitive to moment tensor variations, we have shown those results only in the Supporting Information (Fig. S3) as well as in Fig. 12 and Table S1.

The predicted velocities from GPE only models show a good fit with the observed NNR velocities from Kreemer *et al.* (2014) in the IN–EU collision zone for CRUST1 and LITHO models (Fig. 4, bottom row). LITHO shows very good fit within the entire Tibetan plateau (Fig. 4l), while for CRUST1, the fit degrades in the eastern part of Tarim basin (Fig. 4k). The EHS displays a poor fit for all the models, but the angular misfit is found to be lower for CRUST1 model (Fig. 4k). The fit to NNR velocities is observed to be very poor for CRUST2 model (Fig. 4j). The lowest average regional rms error (∼8.4 mm yr^{-1}) and lowest average angular misfit (∼7.2°) is obtained for CRUST1 model. LITHO shows a slightly higher rms error of ∼10.2 mm yr^{-1} and an angular misfit of ∼11°. The CRUST2 model seems to be underpredicting 4–5 cm of northward directed velocity within the Tibetan plateau, which is much reduced for the CRUST1 model. The LITHO model, on the other hand, seems to be slightly overpredicting the northward component of velocity such that a ∼1 cm yr^{-1} of southward motion is required to fit the observed velocities within the Tibetan plateau (Fig. 4l). An important point to note is that despite the average angular misfit being lowest for CRUST1 model, we observe a better fit to observed velocity directions for LITHO model in central Tibet and Tarim Basin. The rms error and angular misfit between predicted and observed velocities are found to be higher for compensated models than uncompensated models (Fig. 12 and Table S1), with LITHO producing the lowest misfit.

4.2 Predicting parameters using a combined model of GPE and mantle buoyancies

In the previous section, we showed that the GPE derived stresses are able to fit most of the surface constraints as long as we derive the crustal thickness and densities from the CRUST1 and LITHO crustal models, with LITHO model faring slightly better overall. However, in central Tibet, LITHO gives too little E–W extension compared to CRUST1 and hence the match with strain rates degrades for LITHO in this region. CRUST1, on the other hand, predicts the observed E–W extension in central Tibet and yields a good fit with GSRM tensors and $SH_{\max}$ orientations. We also showed that modifying the density of the lithospheric mantle in order to achieve isostatic compensation, did not produce any better results. In this section, we explore what effect does adding the deviatoric stresses from density-driven mantle convection has on the stress pattern in this region and how do these combined stresses compare with the observational constraints.

We take the horizontal tractions predicted from the mantle convection models at ∼100 km depth [τ_{xz} and τ_{yz} in eqs (4) and (5)] and apply them as basal boundary condition in the lithosphere thin sheet model to solve for the horizontal deviatoric stresses (*cf.* Singh & Ghosh 2019). The deviatoric stresses predicted by mantle convection show a dominantly N–S compression within the IN–EU collision zone irrespective of the tomography model used (Fig. 5). The use of SH08 viscosity does not change the stress pattern significantly, hence, for the sake of brevity, we have shown results from

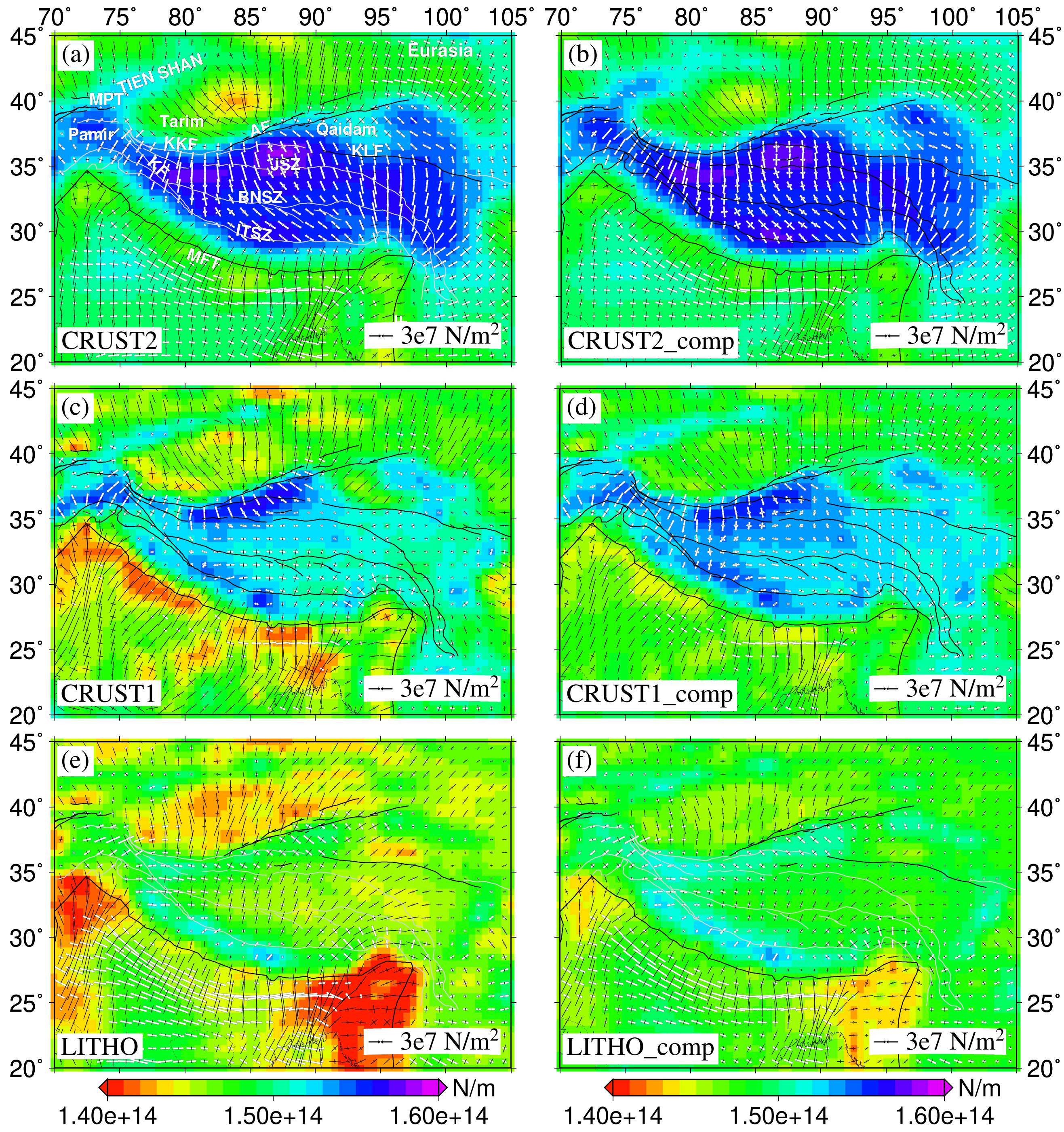

Figure 3. Deviatoric stresses plotted on top of GPE variations derived using densities and thickness from different crustal models. The white arrows denote tensional stresses, and black arrows indicate compressional stresses.

GHW13 viscosity structure only. The results from SH08 viscosity models are shown in Table S1. When these mantle derived deviatoric stresses are added to those derived from GPE variations (Fig. 3), we noted some significant changes (Figs 6–8). The introduction of large compressional stresses from S40RTS and SAW642AN models changes the region of dominant extension as predicted by CRUST2 model to more of a strike-slip regime (Figs 6a, b, e and f). However, in case of hybrid models (SINGH_S40RTS and SINGH_SAW), addition of traction related stresses do not have much effect on the total stress field except for a slight tilting of the NW–SE oriented stress axes to WNW–ESE orientation in central and western Tibet (Figs 6c, d, g and h). This is because the deviatoric stresses predicted by the hybrid models are much smaller in magnitude (Figs 5c and d). The dominant N–S tension in Pamir changes to nearly E–W tension for the hybrid models.

For CRUST1, the mantle convection models introduce a N–S component of compression in central Tibet in addition to E–W extension (Fig. 7). Moreover, the N–S tensional stresses in Pamir re-orient themselves to a more E–W direction, as observed. In case of combined models of CRUST1 and S40RTS/SAW642AN, the

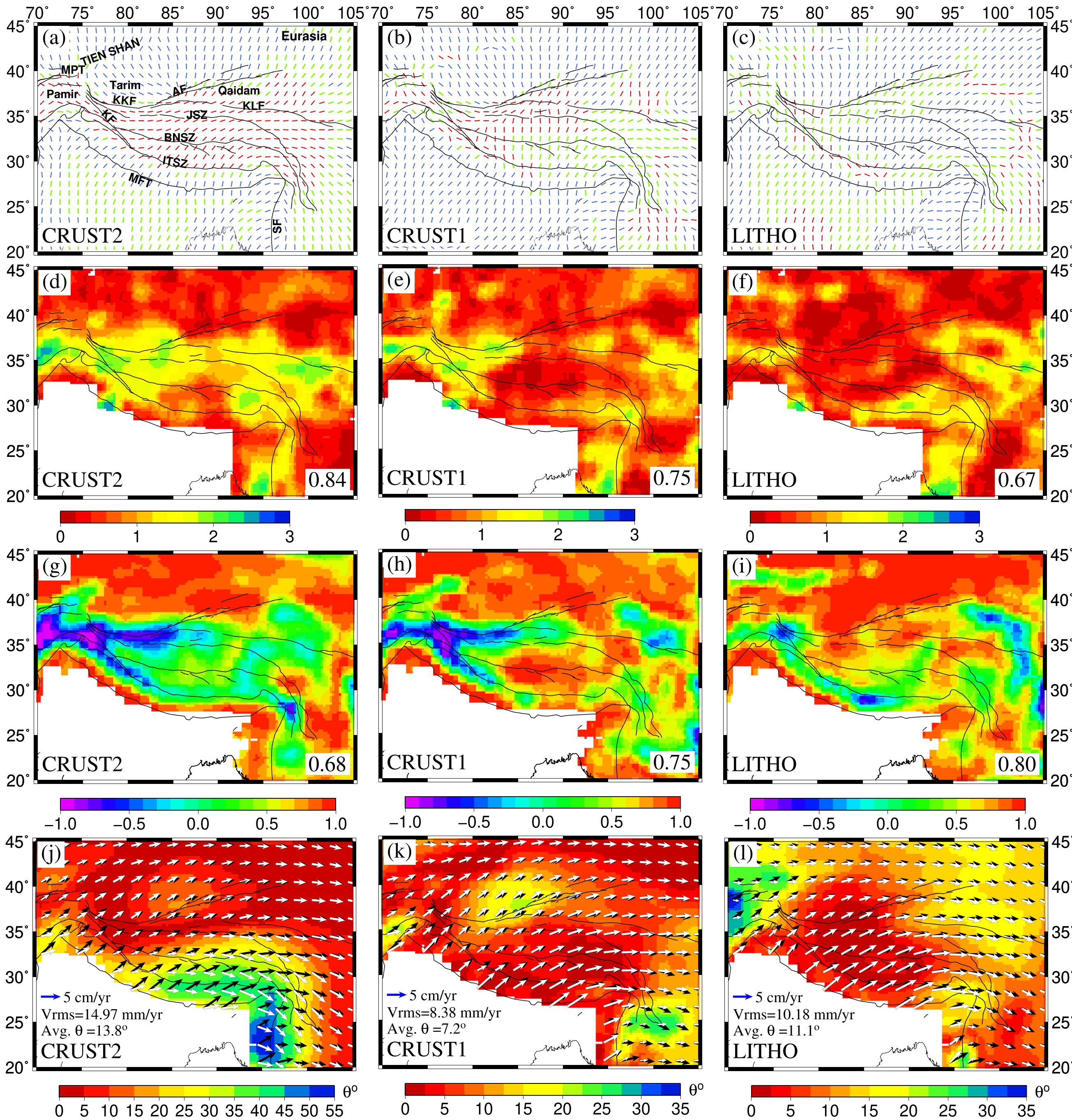

Figure 4. Quantitative comparison of predicted parameters from GPE only models to surface observables. Top row (a–c) shows $SH_{\max}$ predicted from GPE variations derived using densities and thickness from different crustal models, CRUST2 (left-hand panel), CRUST1 (middle panel) and LITHO (right-hand panel). The red lines denote tensional regime, blue is for thrust and green is for strike-slip regime. The second row (d–f) shows the total misfit between observed $SH_{\max}$ directions from WSM (Fig. 2) and predicted $SH_{\max}$ directions shown in the top row. Correlation of predicted deviatoric stresses with strain rate tensors obtained from Kreemer *et al.* (2014) is shown in the third row (g–i). Bottom panel (j–l) shows the predicted plate velocities (white vectors) and observed NNR velocities (black vectors) (Kreemer *et al.* 2014) plotted on top of the angular misfit (θ) between the two. Note the change in scale for CRUST2.

compressional stresses from mantle tractions dominate over GPE derived stresses, thus leading to predominant compression within most of the study region, except for an area near the Altyn-Tagh fault (Figs 7a, b, e and f). On the other hand, the compressional stresses from the hybrid models are comparable in magnitude to the tensional ones derived from GPE; hence central Tibet is found to have strike-slip type of deformation (Figs 7c, d, g and h). The rotation of the compressional stress axes around the EHS is also slightly more pronounced for the hybrid models. In eastern Tibet, the combined stresses show a strike-slip pattern.

As for LITHO, the magnitude of N–S compression as well as E–W tension increases throughout Tibet, when tractions from the hybrid models are added (Figs 8c and d), whereas most of central Tibet shows dominant compressional stresses when tractions from S40RTS or SAW642AN are added (Figs 8a, b, e and f). This is because LITHO alone predicts N–S compression within central

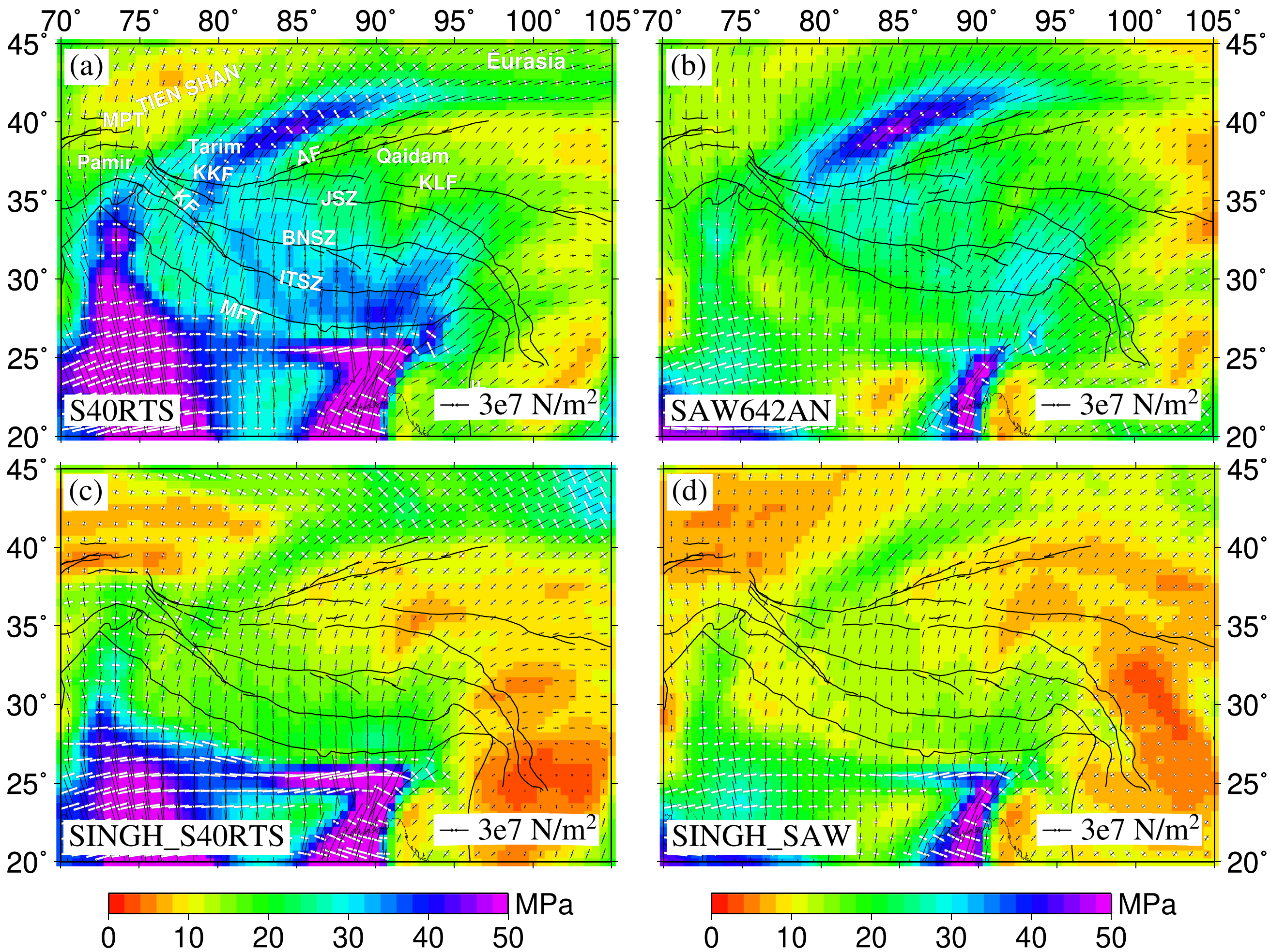

Figure 5. Deviatoric stresses predicted using mantle tractions from various tomography models for GHW13 viscosity structure plotted on top of their second invariants. The black arrows denote compressional stresses and white arrows indicate tensional stresses.

Tibet (Fig. 4c). Adding these to the N–S compressional stresses from mantle tractions enhances the compressional stress magnitudes in that area. The deformation within Pamir changes to pure strike-slip with E–W extension and N–S compression. The magnitude of NE–SW compression across MFT also increases for all the models.

The predicted SH_{max} from the combined models (Figs 6–8, bottom panels) show an improved fit to the observed SH_{max} for all crustal models (Fig. 9). The misfit from the combined stress is lower for all models compared to GPE only models (Fig. 4). The CRUST2 model undergoes a drastic improvement in fit (Fig. 9, left-hand column). Although the LITHO model yields the lowest misfit among the GPE only models, it is the CRUST2 model that shows lowest misfits, when mantle derived basal tractions from S40RTS and SAW642AN are taken into account (Figs 9a, d and 12). However, in case of hybrid models (SINGH_S40RTS and SINGH_SAW), the lowest misfit is observed for CRUST1 (Figs 9h, k and 12), with SINGH_S40RTS+CRUST1 model yielding the lowest value (Fig. 9h).

The correlation of deviatoric stress tensors with observed strain rate tensors improves significantly on adding the contribution from mantle tractions (Figs 10 and 12). Again, there is a drastic improvement for the CRUST2 model (Fig. 10, left-hand column). CRUST2 yields a better fit when mantle tractions from S40RTS or SAW642AN models are added (Figs 10a and d), while CRUST1 yields a higher correlation if we use tractions from the hybrid models (Figs 10h and k). Interestingly, whereas CRUST1 alone shows excellent fit in central Tibet, adding the mantle contribution from S40RTS and SAW642AN degrades the fit in that region (Figs 10b and e). This is because the mantle tractions are adding too much compression in this area (Figs 8e and f). However, the correlation increases significantly in central Tibet for coupled models of CRUST1 and SINGH_S40RTS/SINGH_SAW along with an anti-correlation on the western flanks of the Tibetan plateau near Pamir and KKF (Figs 10h and k). LITHO combined with mantle tractions shows a moderate correlation in both central and western Tibet. Hence, CRUST1 shows the highest correlation when mantle tractions are derived from the hybrid models and CRUST2 performs better when S40RTS or SAW642AN is used to compute traction derived stresses. LITHO does not seem to prefer one model over the other (Fig. 10, right-hand column). The fit is found to be the best for SAW642AN+CRUST2 model with an average correlation of 0.93.

The combined models show better fit to plate velocities compared to GPE only models (Fig. 11). The rms error is almost halved for CRUST2 when the velocities from mantle tractions are added (Fig. 11, left-hand column and Fig. 12). Similar to previous

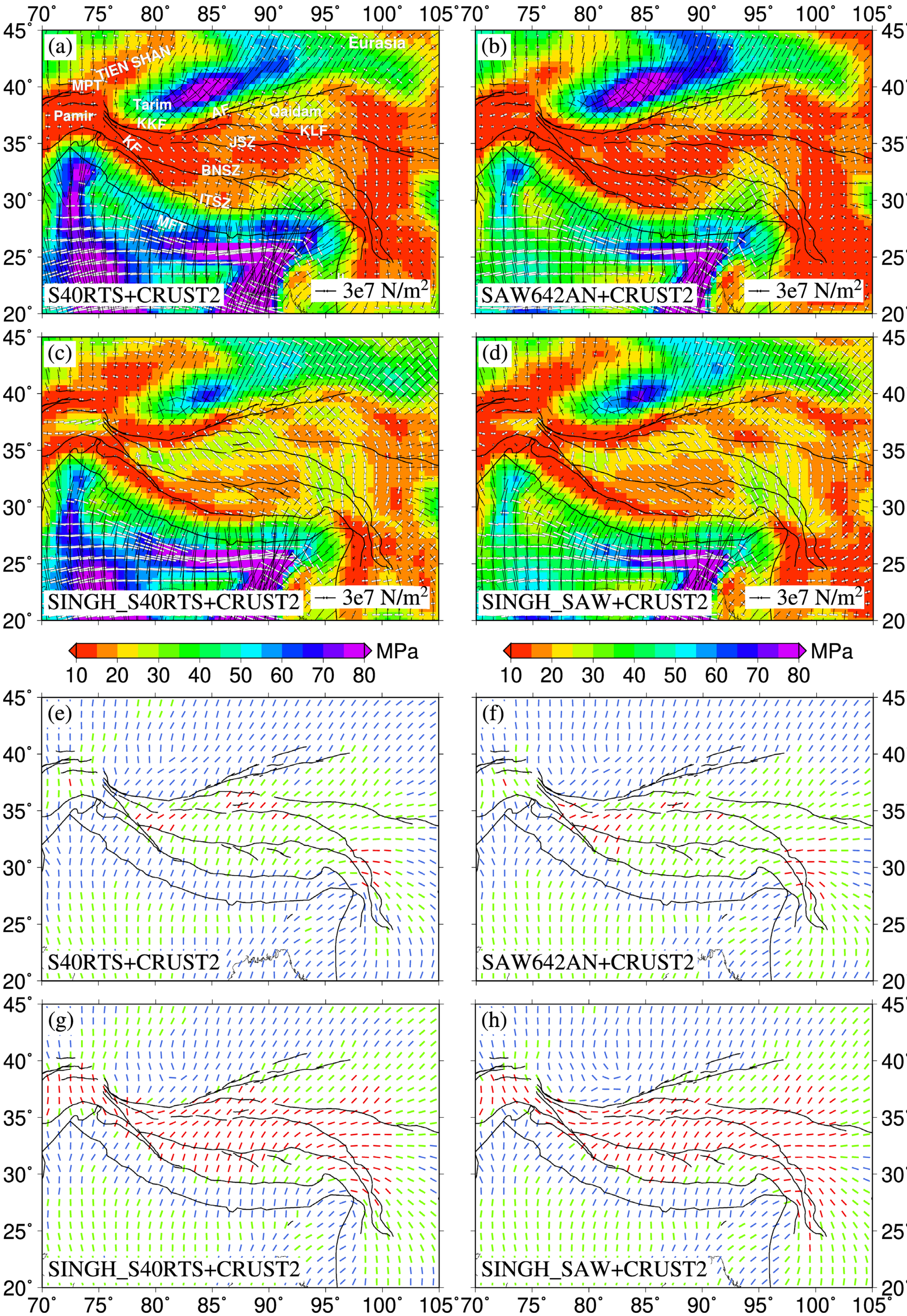

Figure 6. Deviatoric stresses (a–d) predicted using combined effects of GPE computed from CRUST2 and mantle tractions derived from various tomography models plotted on top of their second invariants. The white arrows denote tensional stresses, and black arrows indicate compressional stresses. The bottom panel (e–h) shows $SH_{\max}$ predicted from these models. The red lines denote tensional regime, blue is for thrust and green is for strike-slip regime.

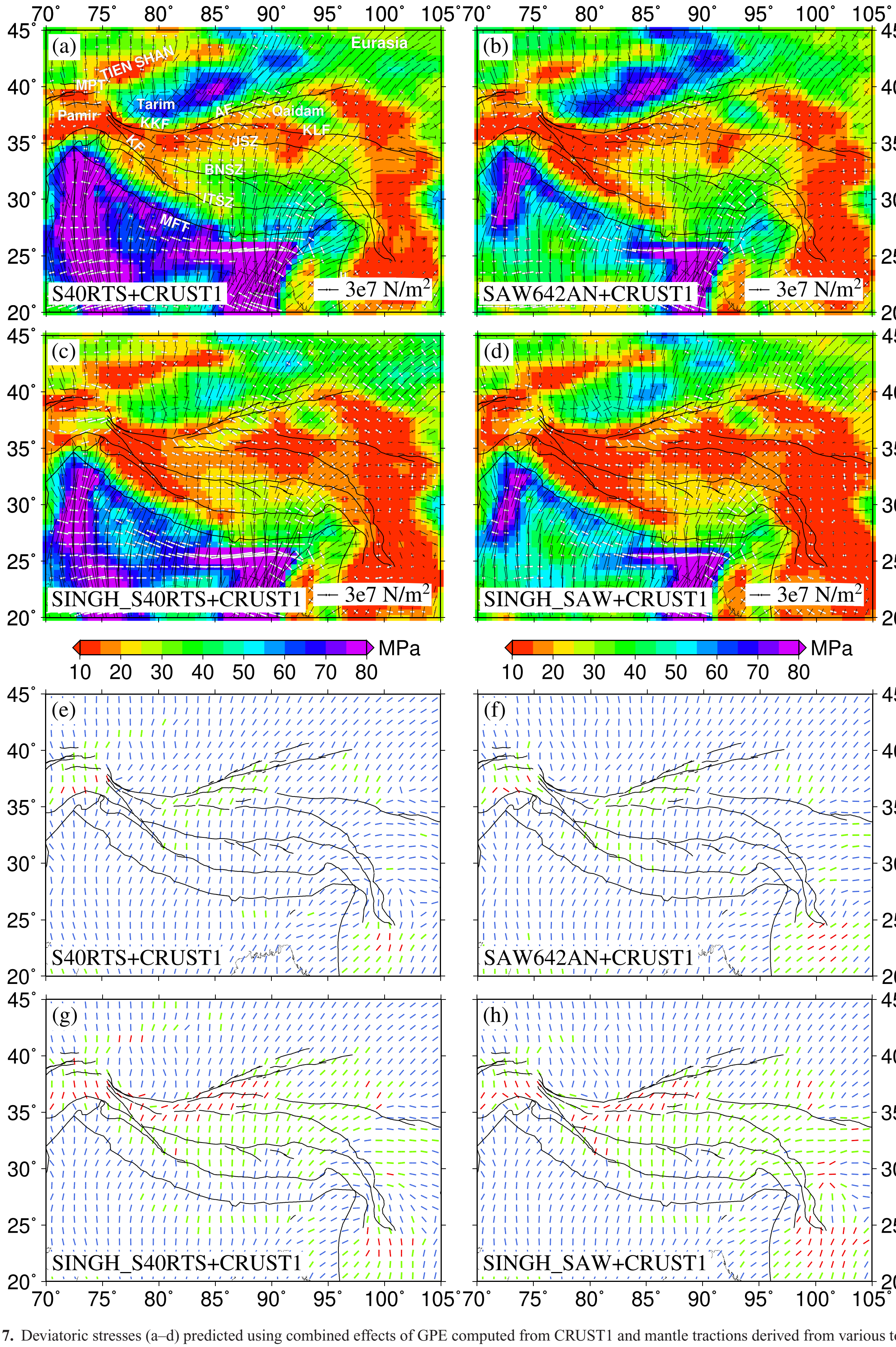

Figure 7. Deviatoric stresses (a–d) predicted using combined effects of GPE computed from CRUST1 and mantle tractions derived from various tomography models plotted on top of their second invariants. The bottom panel (e–h) shows $SH_{\max}$ predicted from these models.

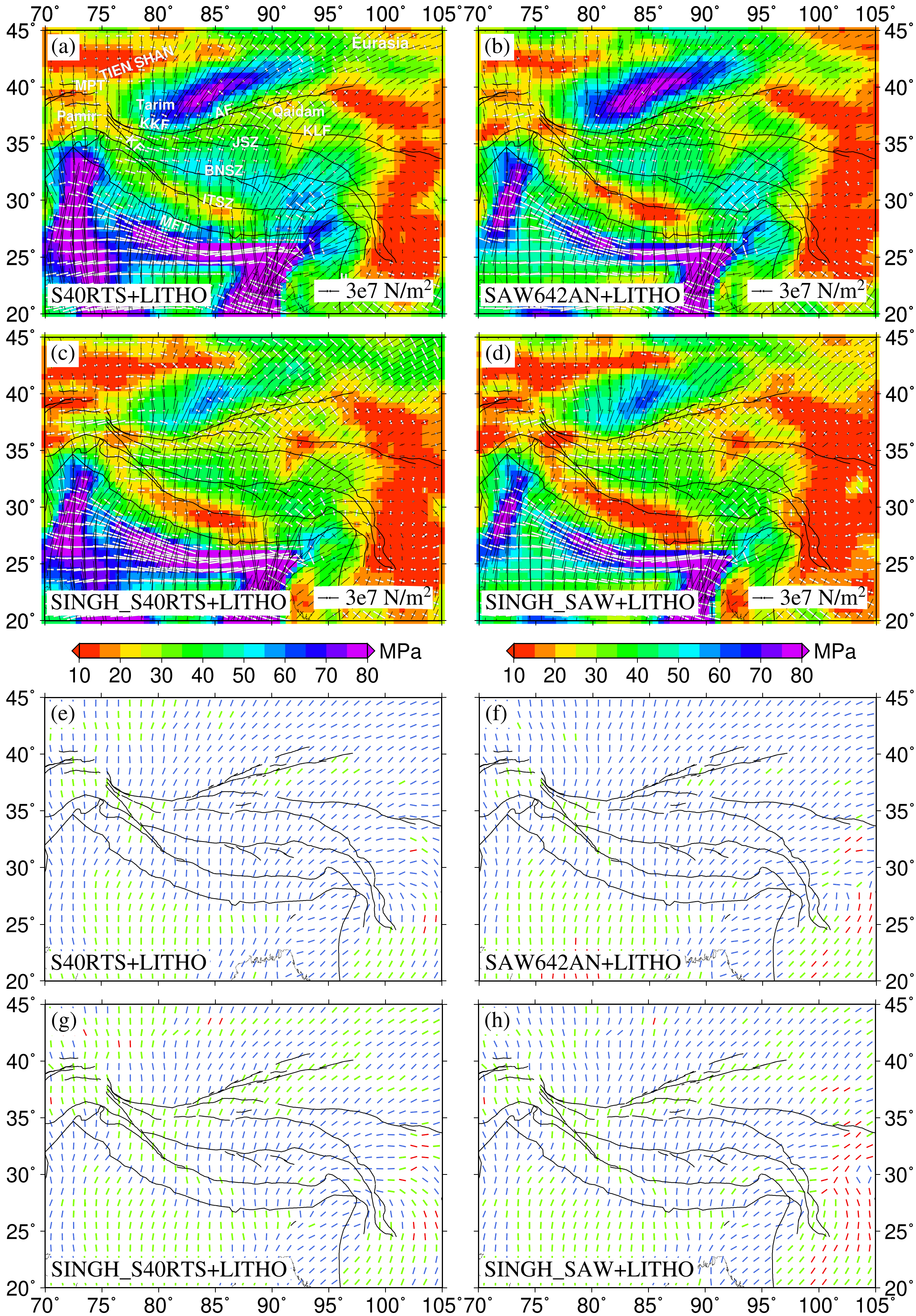

Figure 8. Deviatoric stresses (a–d) predicted using combined effects of GPE computed from LITHO and mantle tractions derived from various tomography models plotted on top of their second invariants. The bottom panel (e–h) shows SH_{max} predicted from these models.

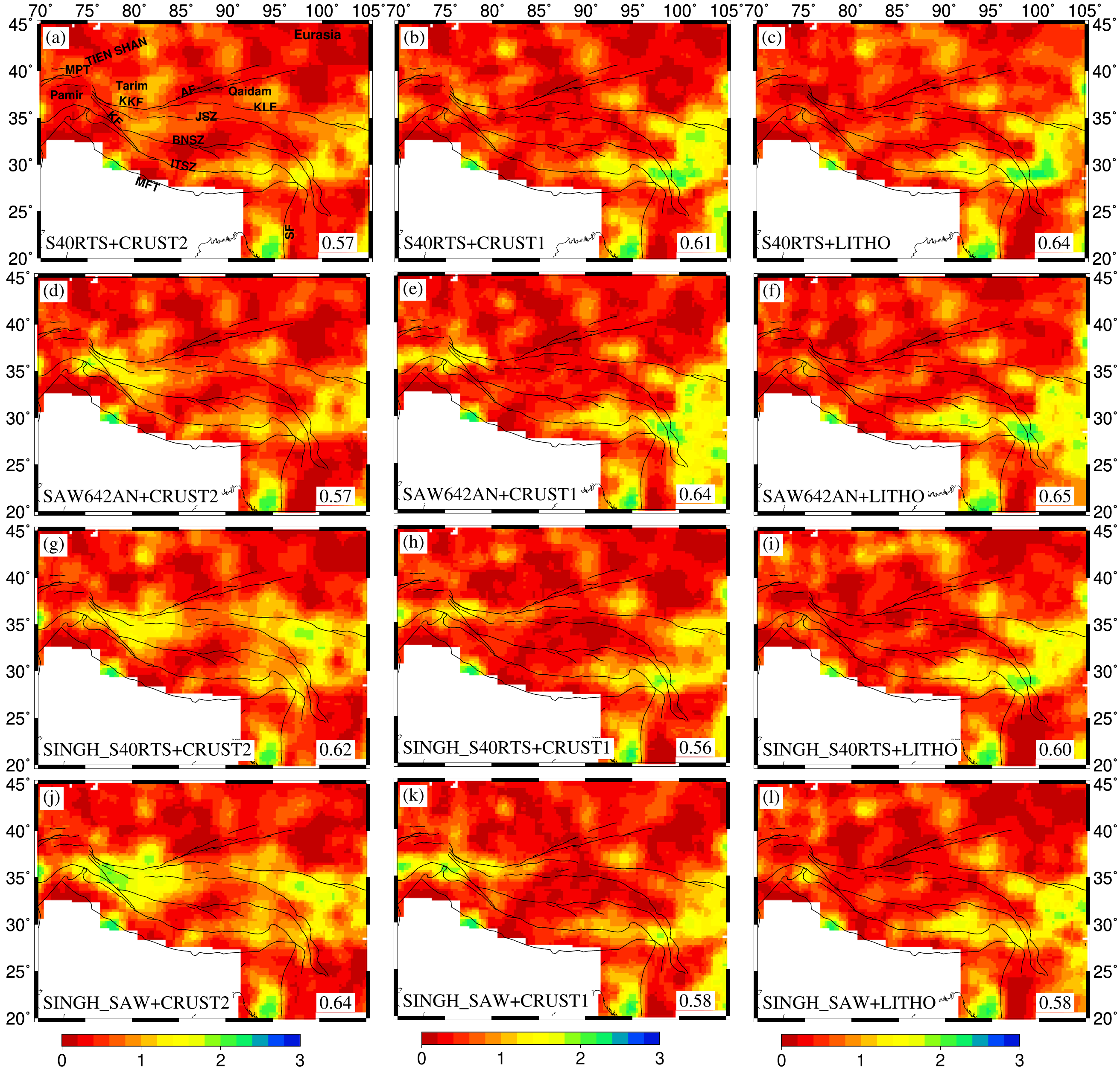

Figure 9. Total misfit between observed SH_{max} from WSM (Heidbach *et al.* 2018) and SH_{max} predicted using combined effects of GPE computed from different crustal models and mantle tractions derived from various tomography models.

constraints, S40RTS and SAW642AN models show much better fit to observed velocities with CRUST2 rather than other two crustal models, while CRUST1 performs better with SINGH_S40RTS model. Moreover, we observe that combined models of LITHO plus mantle tractions show better fit to the orientation of observed velocities than the combined models of CRUST1 and mantle tractions especially towards the east of EHS, even though the average rms error might not always reflect the same. Such behaviour becomes more evident when we look at the angular misfit between observed and predicted velocities, where SAW642AN+CRUST2 yields the lowest average angular misfit of 4° (Fig. 11d). We obtain the lowest regional rms error of ∼5 mm yr^{-1} for SINGH_S40RTS+CRUST1 model (Fig. 11h). Majority of the misfit lies within the Pamir and Tien-Shan region in the west, and the EHS in the east for CRUST1. Within Tibet, the hybrid tomography models predict almost correct velocity for LITHO (Figs 11i and l). Most models seem to be underpredicting a 1–1.5 cm yr^{-1} of southward directed component of velocity around the EHS. The fit seems to degrade significantly for SAW642AN, when coupled with CRUST1 or LITHO models as compared to CRUST2 (Figs 11d–f).

5 DISCUSSION

We had earlier studied the dynamics of the Indian Plate and the IN–EU collision zone by modeling the stresses arising from lithosphere buoyancies as well as mantle tractions acting at the base of the lithosphere (Singh & Ghosh 2019). We had tested various tomography models and had found that the combined deviatoric stresses

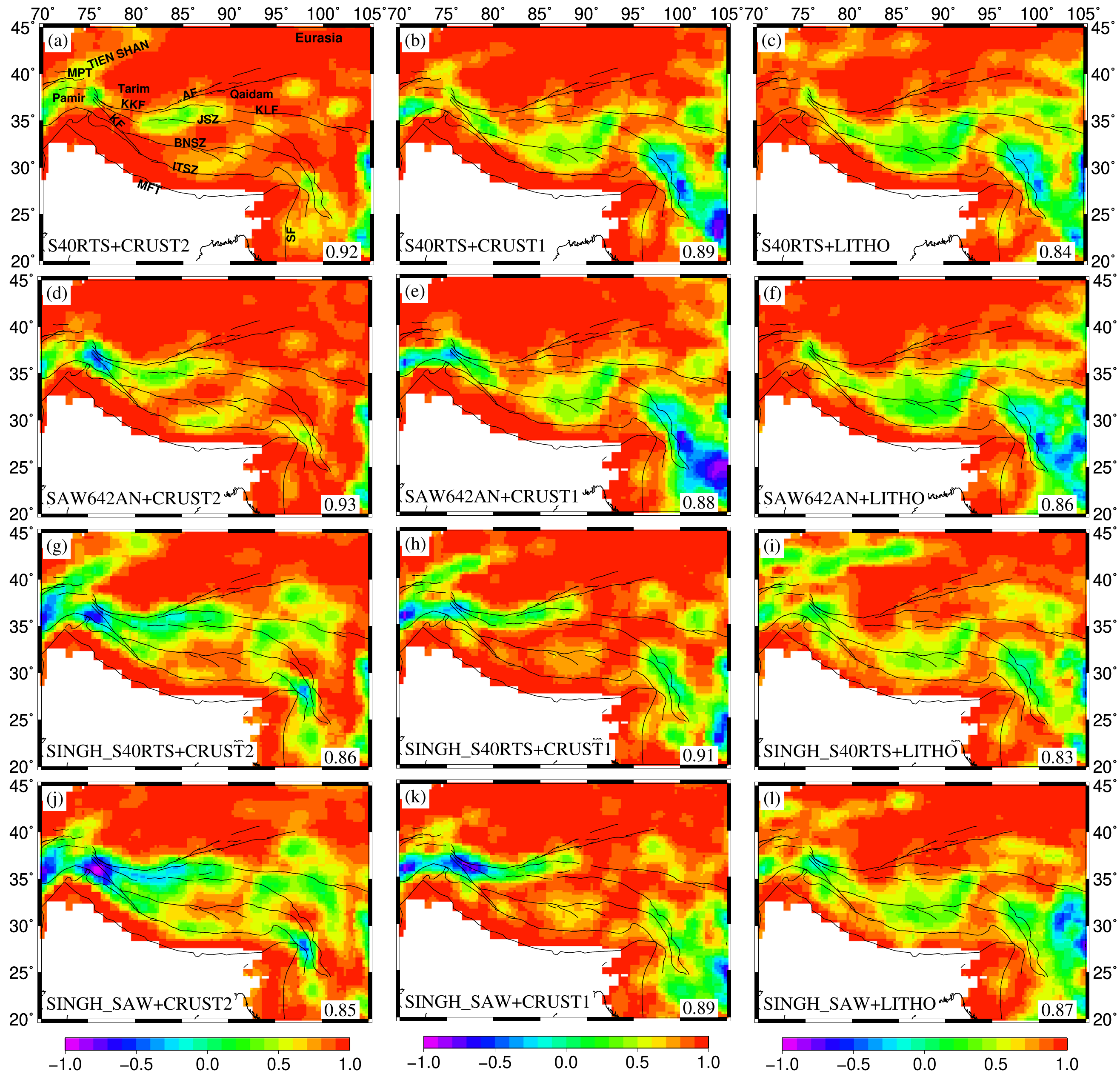

Figure 10. Correlation coefficients between strain rate tensors from Kreemer *et al.* (2014) and deviatoric stress tensors predicted using combined effects of GPE computed from different crustal models and mantle tractions derived from various tomography models.

arising from the regional model of Singh *et al.* (2014) embedded within S40RTS coupled with CRUST1.0 provided the lowest misfit to observed parameters. However, a significant misfit between observed and predicted parameters in the IN–EU collision zone was also found; especially the predicted velocities deviated from the observed ones significantly around the EHS. Also, the correlation with observed strain rates was poor in some parts of the Tibetan plateau. It is common to attribute such misfits to the uncertainties in the mantle tomography models. Afterall, our confidence in the density structure of the lithosphere far exceeds that of the mantle density structure. But, could the inaccuracies in the crustal model (CRUST1.0) have been a possible source of misfit? To address that, in this paper, we tested three crustal models: CRUST1, CRUST2 and LITHO, in order to study the effect of crustal density and thickness on the computation of GPE and the associated deviatoric stresses.

The three models showed considerable difference in density and crustal thickness (Fig. 1). The GPE and the resultant deviatoric stresses differed significantly among the three crustal models. CRUST2 showed large scale N–S tension in Tibet, while mostly strike-slip type of stresses including E–W tension were observed for CRUST1. LITHO predicted strike-slip and N–S compressive stresses in large parts of Tibet. LITHO performed better than both CRUST2 and CRUST1 in fitting the observations of $SH_{\max}$, GSRM strain rates and focal mechanisms (Fig. 12 and Table S1). However, in central Tibet, the observed E–W extension is matched better by CRUST1 (Figs 4e and h). It also matches the velocity in the IN–EU region better than CRUST2 and LITHO. Compensating the models did not offer any improvement over uncompensated models in terms of fitting the observed parameters (Fig. 12 and Table S1). Hence, if we consider the CRUST1 and LITHO models, they alone are largely

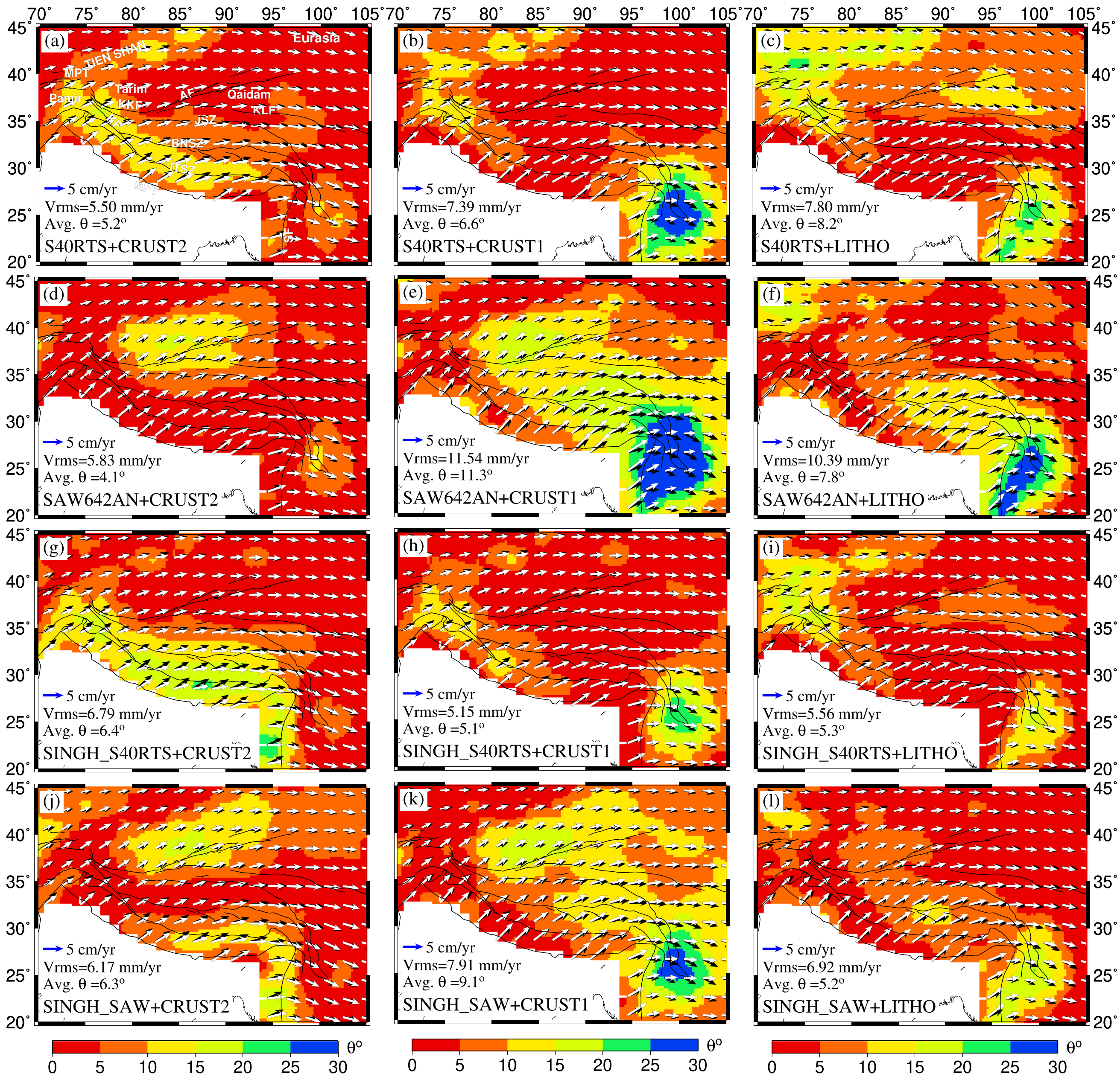

Figure 11. Plate velocities predicted using combined effects of GPE computed from different crustal models and mantle tractions derived from various tomography models plotted on top of angular misfit (θ). Black arrows represent observed NNR velocities (Kreemer *et al.* 2014) and white ones denote predicted velocities.

capable of matching the observational constraints in this region. On the other hand, the predictions from CRUST2 were found to have large misfits, thus demonstrating the inability of CRUST2 model alone to constrain the deformation in this region.

Next, we wanted to test whether adding the deviatoric stresses associated with density driven mantle convection would improve the match with the observational constraints as seen earlier by Ghosh *et al.* (2008, 2013b), since mantle has been suggested to play an important role in this area (Jolivet *et al.* 2018; Ghosh *et al.* 2006). The two best tomography models (S40RTS and SAW642AN) from Singh & Ghosh (2019) were used to calculate tractions using the mantle convection code, HC. We also used two hybrid tomography models, SINGH_S40RTS and SINGH_SAW, obtained after embedding the regional model of Singh *et al.* (2014) in the aforementioned global models. Deviatoric stresses associated with mantle convection showed a dominant N–S compression within the IN–EU collision zone (Fig. 5). These stresses were then added to those obtained from GPE variations to obtain a total stress field (Figs 6–8), which was then compared with surface observations. Adding the contribution from mantle tractions improved the fit to surface observations for all three crustal models, but most prominently for CRUST2. The N–S deviatoric compression from mantle tractions cancelled out the N–S tension predicted by the CRUST2 model, thus improving the match with observations. Especially, both S40RTS and SAW642AN models suggest large scale high velocity anomalies underlying this area that are likely to represent subducted slabs, giving rise to the N–S compressional stresses. Thus, the CRUST2 model requires a much more prominent contribution from mantle convection. However, the

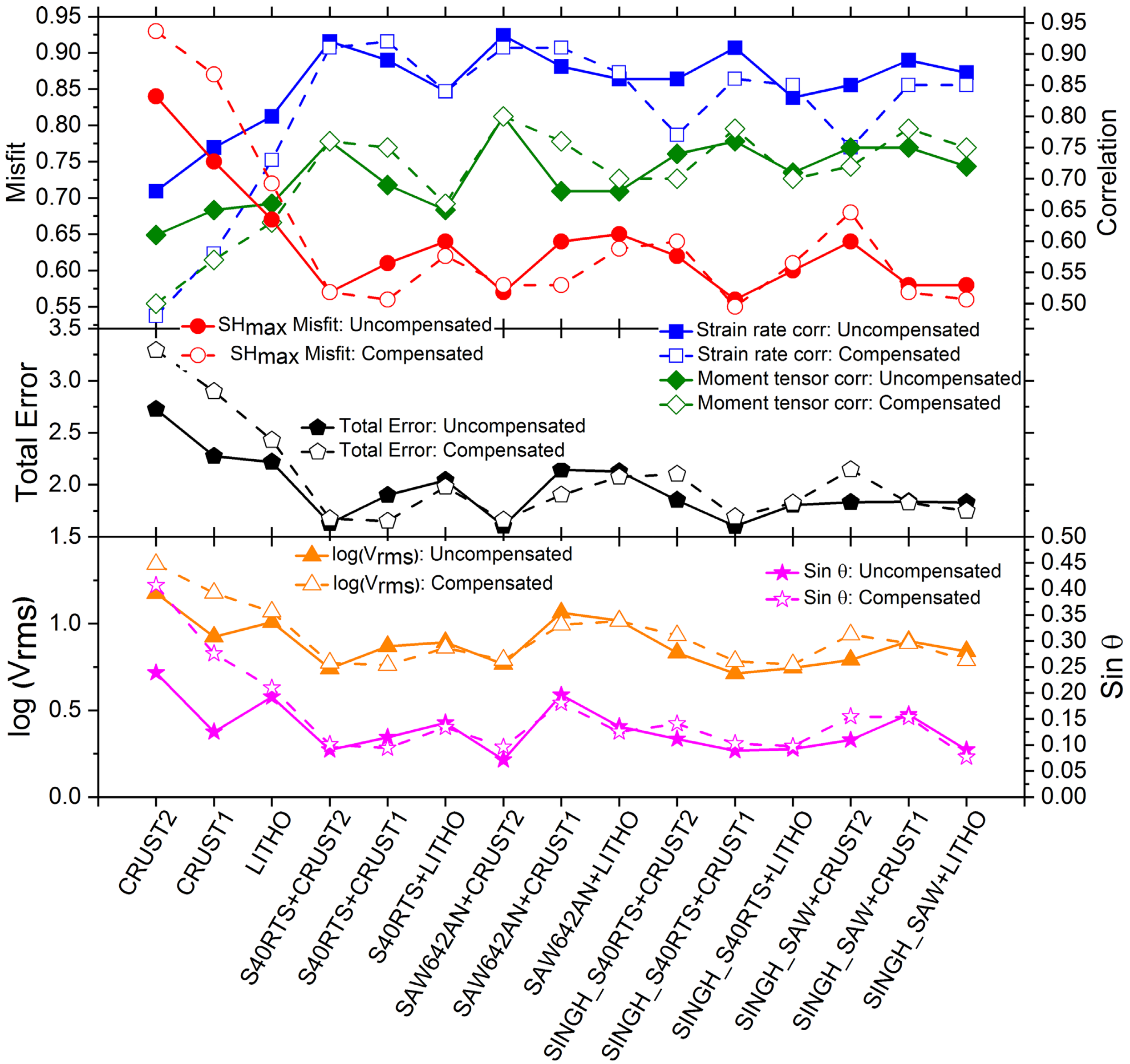

Figure 12. Top panel shows plot of the correlation and misfits between observations and predictions for various models. The solid symbols represent uncompensated models, while open symbols are used for compensated models. Red represents the misfit between observed and predicted SH_{max}, while blue and green show the correlation of predicted deviatoric stress tensors with GSRM strain rates and moment tensors, respectively. The middle panel shows plot of total error for different models. The bottom panel shows log of rms error (orange) and sine of angular misfits (θ) (magenta) between observed and predicted velocities.

deviatoric stresses predicted by CRUST1 and LITHO were already close to the observed deviatoric stresses and hence these models did not undergo as dramatic an improvement in fit as CRUST2. Hence, although CRUST1 and LITHO require the contribution from mantle to fit the observed parameters, the amount and scale is smaller than that required by CRUST2.

We define a parameter to denote the total error exhibited by the models as below:

$$Total\ Error = (1 - Corr_{\mathrm{GSRM}}) + (1 - Corr_{\mathrm{CMT}}) + \log(V_{\mathrm{rms}}) + \epsilon_p \quad (8)$$

(*cf.* Wang *et al.* 2015; Singh & Ghosh 2019) that takes into account the fit with all constraints. Here, $Corr_{\mathrm{GSRM}}$ is the average correlation with strain rate tensors, $Corr_{\mathrm{CMT}}$ is the average correlation with moment tensors, V_{rms} is the RMS error between the predicted and observed plate velocities and ϵ_p is the total misfit between predicted and observed SH_{max} which had been defined previously as $\sin\theta(1+R)$. The values obtained for all models are summarized in Table S1 and in Fig. 12. We found that the combined model of CRUST1 and SINGH_S40RTS using GHW13 viscosity structure (SINGH_S40RTS+CRUST1) gave the best fit out of all the models (total error 1.60), though SAW642AN+CRUST2 and S40RTS+CRUST2 also came close (total errors 1.61 and 1.63, respectively). Among the GPE only models, CRUST2 shows the highest error (∼2.7–3.3), whereas LITHO yields the lowest error (∼2.4). The use of SH08 viscosity structure leads to higher errors (>2) for most models.

The models predicting strike-slip type of deformation in the IN–EU collision zone show the best fit to observed constraints. For example, CRUST2 predicts dominant tensional stresses within Tibet owing to high GPE. Addition of large N–S compressional stresses from S40RTS and SAW642AN tomography models cancel out the N–S tension and what is left is strike-slip deformation (Figs 6a, b, e and f), which yields good fit to observations. On the other hand, the compressional stresses predicted by hybrid tomography models of SINGH_S40RTS and SINGH_SAW are smaller in magnitude than the deviatoric extension predicted by CRUST2 and hence, the coupled models still predict an extensional regime in this area (Figs 6c, d, g and h). Compared to CRUST2, CRUST1 predicts lower GPE and smaller strike-slip deviatoric stresses in this area. When large compressional stresses from S40RTS and SAW642AN are added to these, it leads to overall compression (Figs 7a, b, e and f). Adding the deviatoric stresses from the hybrid models to the deviatoric stresses from CRUST1 retains their strike-slip nature (Figs 7c, d, g and h). In case of GPE only models, LITHO provides an overall better fit to observed parameters, especially in the western part of the plateau, near Pamir, Karakorum fault and Karakax fault (KKF) where it predicts the observed E–W extension. However, in the central and southern parts of the Tibetan plateau, CRUST1 fares better as it predicts the observed E–W extension whereas LITHO produces N–S compression (Fig. 4, top row). Adding the contribution from mantle tractions introduces slightly higher E–W extension and N–S compression, improving the fit almost everywhere for both CRUST1 and LITHO models. The N–S compression in central Tibet is still too large for LITHO (Fig. 8).

We also compute the strain rates based on the predicted deviatoric stresses. As mentioned earlier, our FE model predicts the relative strain rates, which need to be multiplied with a scaling factor (the same factor that was used to obtain the velocity magnitudes) to get the absolute strain rates (*cf.* Ghosh *et al.* 2019). All crustal models predict high strain rates along the Himalayas ($>200 \times 10^{-9}$), with large NE–SW compression (Fig. 13, left-hand column). Such high strain rates are also observed along both the eastern and western syntaxes. The pattern of strain rates are similar to the corresponding deviatoric stresses (Fig. 3). Both CRUST2 and LITHO models suggest higher deformation in north-central Tibet (strain rates are $\sim 50 \times 10^{-9}$ or higher), while CRUST1 predicts much lower strain rates in this area. In order to quantify the type of deformation needed for matching the GSRM strain rates (Fig. 2a), we subtract the strain rates predicted by the crustal models (Fig. 13, left-hand column) from the GSRM strain rates. These residual strain rates give an indication as to how much and what kind of strain is required from the mantle contribution to fit the GSRM strain rates. We find that strain rates predicted by CRUST2 require a large amount of compression to match the GSRM strain rates (Fig. 13b), as evident by the drastic improvement in fit to observations on adding large compressional stresses from S40RTS and SAW642AN models. The strain rates predicted by CRUST1 suggest that it requires large compressional strain in western Tibet to match the observed deformation (Fig. 13d). Mantle convection models predict large compression within this area due to subducted slabs in the underlying mantle, hence adding the contribution from mantle convection models improves the fit significantly (Figs 9–10, middle column). On the other hand, in central Tibet CRUST1 requires very small strain to match the GSRM strain rates (Fig. 13d). As LITHO predicts large N–S compression within central Tibet (Fig. 13e), extension is required that can reduce/cancel out the compression in order to match the observed deformation (Fig. 13f). However, the mantle convection models do not predict extension in this area, hence no significant changes are observed for LITHO model in central Tibet on adding the contribution from mantle. Both CRUST1 and LITHO require extension around the EHS to match the observed strain rates, as both models predict this area to be in thrust regime. Thus, the GPE only models require significant contribution from mantle in order to match the observed deformation.

To understand the relative contribution of both the sources of deviatoric stress, we calculate the ratio of their second invariants (Fig. 14). For each crustal model, the corresponding tomography model that yields the best fit to observations is used. For CRUST2 and SAW642AN, the relative magnitude of GPE versus mantle related stresses shows a dominant contribution of stresses associated with mantle convection, prominently at the flanks of the Tibetan plateau, whereas within central Tibet, they are almost equivalent in magnitude (Fig. 14a). In case of CRUST1 and SINGH_S40RTS, mantle plays a dominant role in central Tibet, while to the north and around EHS, GPE contribution is much larger (Fig. 14b). For compensated LITHO and SINGH_SAW, the combined stresses from which show the least misfit out of all LITHO models, the GPE related stresses are found to be smaller compared to those from mantle convection in Tibet (Fig. 14c).

We compare our predicted velocities with the actual GPS velocities with respect to a fixed Eurasian Plate (Fig. 15). The observed GPS vectors are obtained from Kreemer *et al.* (2014) and Zheng *et al.* (2017). We have used Kreemer *et al.* (2014) as the primary source of GPS vectors and Zheng *et al.* (2017) for additional datapoints. CRUST2 shows a good fit to the observed GPS vectors in Tibetan plateau when combined with S40RTS and SAW642AN models including the rotation of velocity vectors around EHS (Figs 15a and b). On the other hand, CRUST1 and LITHO predict velocities close to the observed velocities when combined with SINGH_S40RTS model (Fig. 15c). However, significant misfits are observed near EHS. SAW642AN+CRUST2 shows the least misfit with GPS velocities in this area (Fig. 15b).

6 CONCLUSION

Understanding the forces behind deformation has been a long-term goal for the Geodynamics community. Complex regions, such as the IN–EU collision zone, pose special challenges due to their remoteness, paucity of data and the very nature of deformation itself. Our goal in this paper has been to understand the forces behind deformation in the IN–EU collision zone and also to quantify the relative contribution of lithosphere versus mantle forces depending on the crustal model used. Inaccuracies in determining lithosphere structure (density and thickness) will lead to inaccuracies in estimating the relative contribution of these forces. Hence, an accurate crustal model is essential when trying to understand deformation. We saw that our conclusions are different based on which crustal model we chose. CRUST2 requires a larger contribution from mantle tractions to match the deformation indicators in this region compared to the two more recent crustal models. However, it is important to note that all three crustal models require contribution from deeper high density anomalies in the mantle, most likely originating from Tethyan subduction (Becker & Faccenna 2011), which promote downwelling and generate dominant compressive stresses in this region, to better fit the surface observations.

We would also like to emphasize that it is important to use more than one observational constraint when attempting to infer the dynamics of a particular region. It has been shown earlier by Ghosh *et al.* (2013b) how using a single observational constraint can lead

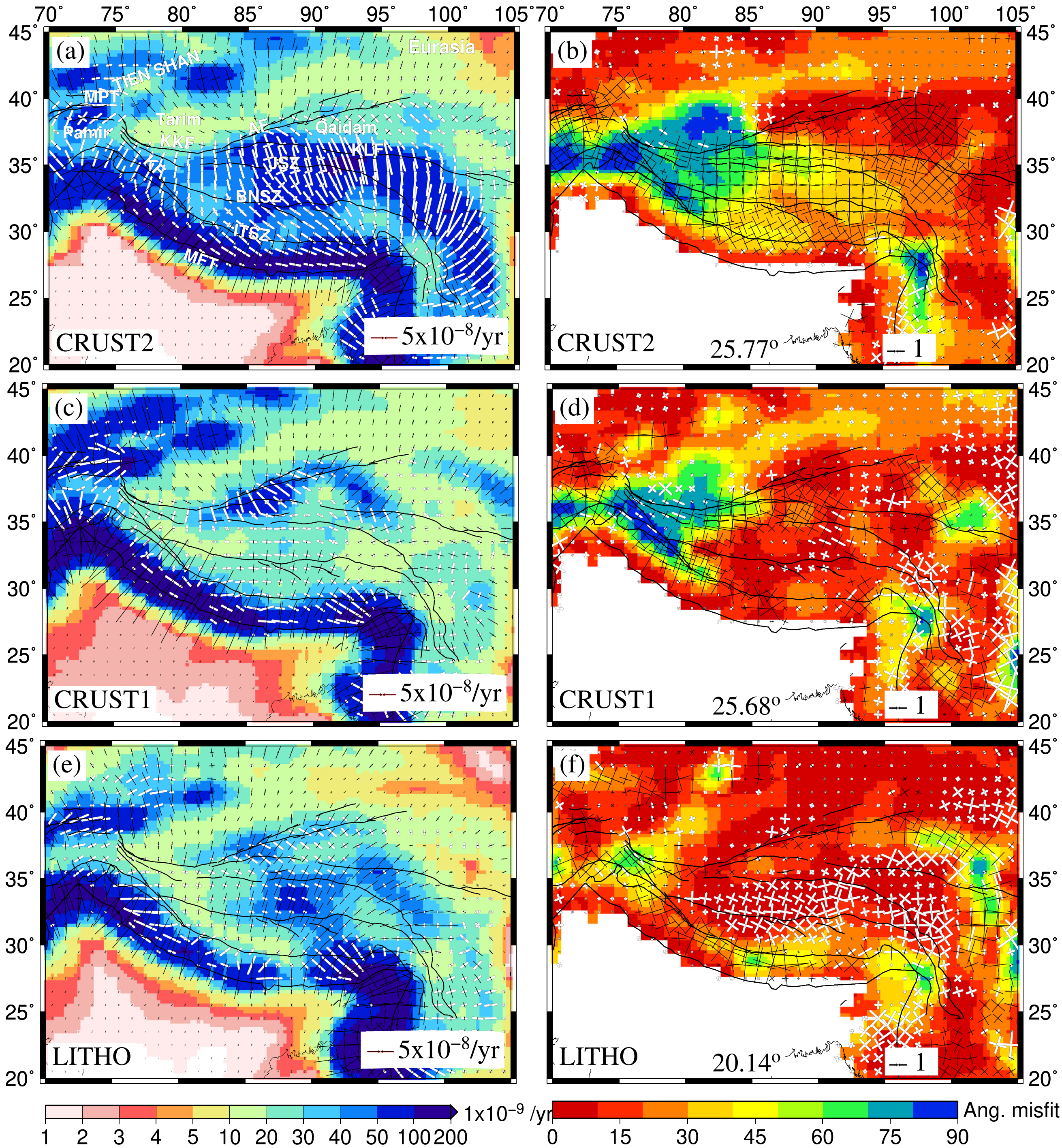

Figure 13. Strain rates predicted from GPE only models plotted on top of their second invariants. The black arrows denote compression and white arrows represent extension. (Middle) Difference between GSRM strain rates and those predicted by GPE models plotted on top of the angular misfit between predicted and observed most compressional strain axes. The arrows on top represent the type of deformation required to match the observed strain rates (Fig. 2a). The magnitudes of these arrows are scaled by the difference in regime (R) between observed and predicted strain rates.

to incorrect conclusions. Hence, in this study we use various data sets (WSM, GSRM, CMT solutions, GPS velocities) to infer about the source of deformation in this area. Recently, Bischoff & Flesch (2018a, b) have tried to explain the deformation in this region using high resolution 3-D models of crustal structure. They have argued that a low viscosity channel within the lower crust is essential to match GPS velocities in this region, especially the rotation of velocity vectors around the EHS. We can match the velocity in this region considerably well, including the fanning of velocity vectors around EHS without invoking lower crustal flow (Fig. 15). Our study does not rule out the existence of lower crustal flow in the region, but demonstrates that it may not be essential for matching the velocities and other deformation indicators. Our results indicate that there is still more work to be done to come up with an accurate and reliable global crustal model. More accurate crustal as well as tomography models of the region would likely improve the results and help us understand the nature of deformation in this very complex region of the Earth.

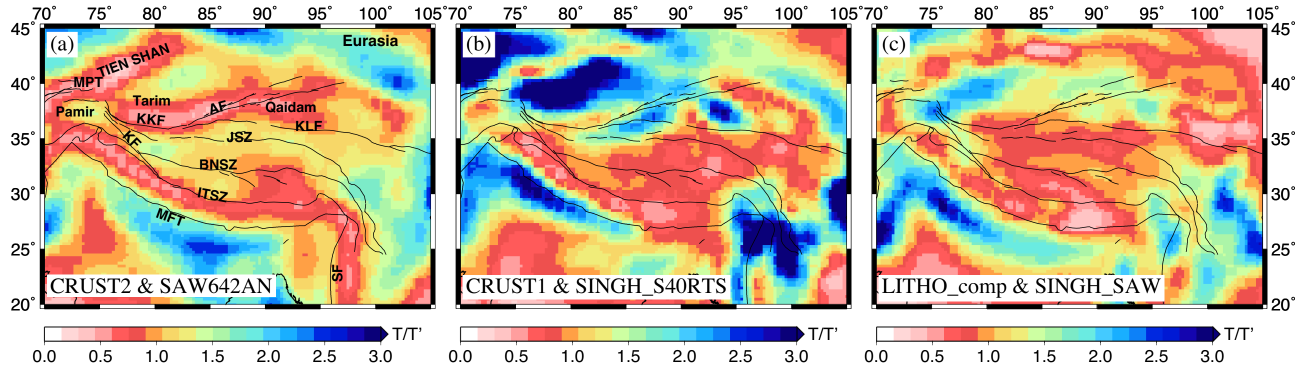

Figure 14. The ratio of the second invariant of deviatoric stresses (T/T'). T stands for the second invariant of deviatoric stresses fom GPE whereas T' stands for those from mantle tractions.

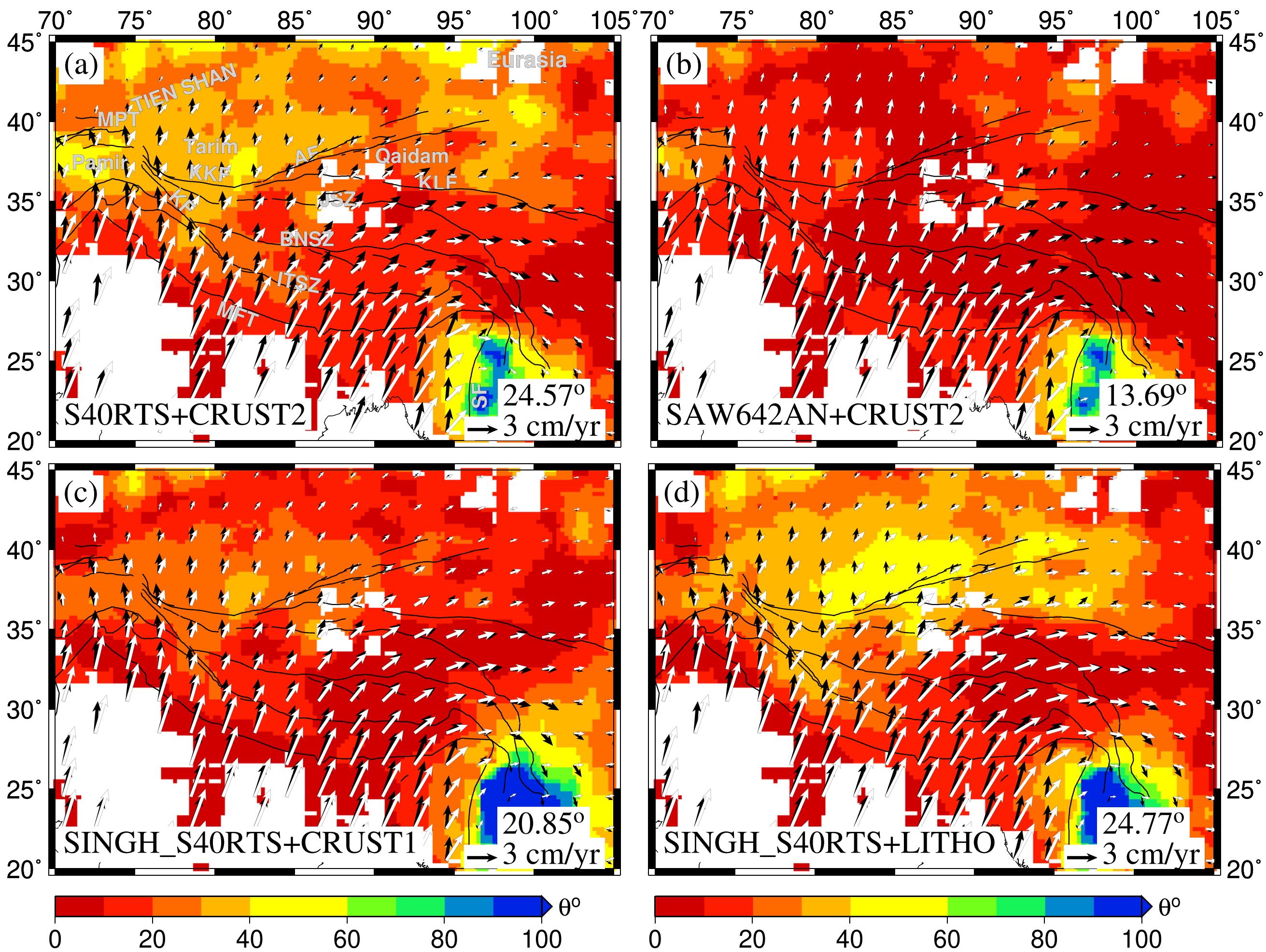

Figure 15. Comparison of observed GPS vectors (black arrows) from Kreemer *et al.* (2014) & Zheng *et al.* (2017) and modeled velocities with respect to a fixed Eurasian Plate (white arrows) using combined effects of GPE computed from different crustal models and mantle tractions derived from different tomography models. The angular deviation between the vectors (θ) are plotted in the background. The average regional angular deviation is noted in the bottom right-hand side of each subfigure.

ACKNOWLEDGEMENTS

We would like to acknowledge F. Capitanio and an anonymous reviewer for their comments that substantially improved the manuscript. We would like to thank C. Kreemer for sharing the GSRM data. We are also grateful to L.M. Flesch and W.E. Holt for insightful discussions. We acknowledge T.W. Becker for the mantle convection code, HC and the Shansyn package. Figures were prepared using GMT 4.5.11 by P. Wessel and W.F. Smith. S. Singh was funded by UGC grant F.No. 2-99/1998(SA-I).

REFERENCES

Artyushkov, E.V., 1973. Stresses in the lithosphere caused by crustal thickness inhomogeneities, *J. geophys. Res.,* **78**(32), 7675–7708.

Becker, T.W . & Faccenna, C., 2011. Mantle conveyor beneath the Tethyan collisional belt, *Earth planet. Sci. Lett.,* **310**(3), 453–461.

Bilham, R. & England, P., 2001. Plateau 'pop-up' in the great 1897 Assam earthquake, *Nature,* **410**(6830), 806–809.

Bischoff, S. & Flesch, L.M., 2018a. Impact of lithospheric strength distribution on India-Eurasia deformation from 3-D geodynamic models, *J. geophys. Res.,* **124** (1), 1084–1105.

Bischoff, S.H. & Flesch, L.M., 2018b. Normal faulting and viscous buckling in the Tibetan plateau induced by a weak lower crust, *Nat. Commun.,* **9**(1), 4952.

Capitanio, F.A., 2020. Current deformation in the Tibetan plateau: a stress gauge in the India-Asia collision tectonics, *Geochem. Geophys. Geosyst.,* **21**(2), e2019GC008649, doi:10.1029/2019GC008649

Dziewonski, A., Chou, T.A. & Woodhouse, J.H., 1981. Determination of earthquake source parameters from waveform data for studies of global and regional seismicity, *J. geophys. Res.,* **86**(B4), 2825–2852.

Ekström, G., Nettles, M. & Dziewoński, A.M., 2012. The global cmt project 2004–2010: centroid-moment tensors for 13,017 earthquakes, *Phys. Earth planet. Inter.,* **200,** 1–9.

England, P. & Houseman, G., 1986. Finite strain calculations of continental deformation: 2. Comparison with the india-asia collision zone, *J. geophys. Res.,* **91**(B3), 3664–3676.

England, P. & Houseman, G., 1989. Extension during continental convergence, with application to the Tibetan plateau, *J. geophys. Res.,* **94**(B12), 17 561–17 579.

England, P. & Houseman, G.A., 1988. The mechanics of the Tibetan plateau, *Phil. Trans. R. Soc. Lond., A,* **326**(1589), 301–320.

England, P. & McKenzie, D., 1982. A thin viscous sheet model for continental deformation, *Geophys. J. Int.,* **70**(2), 295–321.

England, P. & McKenzie, D., 1983. Correction to: a thin viscous sheet model for continental deformation, *Geophys. J. Int.,* **73**(2), 523–532.

England, P. & Molnar, P., 1997. Active deformation of Asia: from kinematics to dynamics, *Science,* **278**(5338), 647–650.

Finzel, E.S., Flesch, L.M., Ridgway, K.D., Holt, W.E. & Ghosh, A., 2015. Surface motions and intraplate continental deformation in Alaska driven by mantle flow, *Geophys. Res. Lett.,* **42**(11), 4350–4358.

Flesch, L.M., Haines, A.J. & Holt, W.E., 2001. Dynamics of the India-Eurasia collision zone, *J. geophys. Res.,* **106**(B8), 16 435–16 460.

Flesch, L.M., Holt, W.E., Haines, A.J., Wen, L. & Shen-Tu, B., 2007. The dynamics of western North America: stress magnitudes and the relative role of gravitational potential energy, plate interaction at the boundary and basal tractions, *Geophys. J. Int.,* **169**(3), 866–896.

Ghosh, A. & Holt, W.E., 2012. Plate motions and stresses from global dynamic models, *Science,* **335**(6070), 838–843.

Ghosh, A., Holt, W.E., Flesch, L.M. & Haines, A.J., 2006. Gravitational potential energy of the Tibetan plateau and the forces driving the Indian plate, *Geology,* **34**(5), 321–324.

Ghosh, A., Holt, W.E., Wen, L., Haines, A.J. & Flesch, L.M., 2008. Joint modeling of lithosphere and mantle dynamics elucidating lithosphere-mantle coupling, *Geophys. Res. Lett.,* **35,** doi:10.1029/2008GL034365.

Ghosh, A., Holt, W.E. & Flesch, L.M., 2009. Contribution of gravitational potential energy differences to the global stress field, *Geophys. J. Int.,* **179**(2), 787–812.

Ghosh, A., Becker, T.W. & Humphreys, E.D., 2013a. Dynamics of the North American continent, *Geophys. J. Int.,* **194**(2), 651–669.

Ghosh, A., Holt, W.E. & Wen, L., 2013b. Predicting the lithospheric stress field and plate motions by joint modeling of lithosphere and mantle dynamics, *J. geophys. Res.,* **118**(1), 346–368.

Ghosh, A., Thyagarajulu, G. & Steinberger, B., 2017. The importance of upper mantle heterogeneity in generating the indian ocean geoid low, *Geophys. Res. Lett.,* **44**(19), 9707–9715.

Ghosh, A., Holt, W.E. & Bahadori, A., 2019. Role of large scale tectonic forces in intraplate earthquakes of central and eastern North America, *Geochem. Geophys. Geosyst.,* **20** (4), 2134–2156

Hager, B.H. & O'Connell, R.J., 1981. A simple global model of plate dynamics and mantle convection, *J. geophys. Res.,* **86**(B6), 4843–4867.

Heidbach, O. *et al.*, 2018. The world stress map database release 2016: crustal stress pattern across scales, *Tectonophysics,* **744,** 484–498.

Hirschberg, H.P., Lamb, S. & Savage, M.K., 2018. Strength of an obliquely convergent plate boundary: lithospheric stress magnitudes and viscosity in New Zealand, *Geophys. J. Int.,* **216**(2), 1005–1024.

Houseman, G. & England, P., 1986. A dynamical model of lithosphere extension and sedimentary basin formation, *J. geophys. Res.,* **91**(B1), 719–729.

Islam, M.S., Shinjo, R. & Kayal, J., 2011. Pop-up tectonics of the Shillong plateau in northeastern India: insight from numerical simulations, *Gondw. Res.,* **20**(2-3), 395–404.

Jay, C.N., Flesch, L.M. & Bendick, R.O., 2017. Kinematics and dynamics of the Pamir, Central Asia: quantifying surface deformation and force balance in an intracontinental subduction zone, *J. geophys. Res.,* **122**(6), 4741–4762.

Jolivet, L., Faccenna, C., Becker, T., Tesauro, M., Sternai, P. & Bouilhol, P., 2018. Mantle flow and deforming continents: From india-asia convergence to pacific subduction, *Tectonics,* **37**(9), 2887–2914.

Kreemer, C., Blewitt, G. & Klein, E.C., 2014. A geodetic plate motion and global strain rate model, *Geochem. Geophys. Geosyst.,* **15**(10), 3849–3889.

Laske, G., Masters, G. & Reif, C., 2001. Crust2.0: a new global crustal model at 2× 2 degrees, http://mahi.ucsd.edu/Gabi/rem.dir/crust/crust2.html.

Laske, G., Masters, G., Ma, Z. & Pasyanos, M., 2013. Update on crust1.0 - a 1-degree global model of earths crust, *Geophys. Res. Abstr,* **15,** 2658.

Liu, M. & Yang, Y., 2003. Extensional collapse of the Tibetan plateau: results of three-dimensional finite element modeling, *J. geophys. Res.,* **108**(B8), doi:10.1029/2002JB002248.

Mégnin, C. & Romanowicz, B., 2000. The three-dimensional shear velocity structure of the mantle from the inversion of body, surface and higher-mode waveforms, *Geophys. J. Int.,* **143**(3), 709–728.

Milner, K., Becker, T.W., Boschi, L., Sain, J., Schorlemmer, D. & Waterhouse, H., 2009. New software framework to share research tools, *EOS, Trans. Am. Geophys. Un.,* **90**(12), 104–104.

Mohadjer, S. *et al.*, 2010. Partitioning of India-Eurasia convergence in the Pamir-Hindu kush from gps measurements, *Geophys. Res. Lett.,* **37**(4), doi:10.1029/2009GL041737.

Molnar, P. & Lyon-Caen, H., 1988. Some simple physical aspects of the support, structure, and evolution of mountain belts, *Proc. Continent. Lithospher. Deform.,* **218,** 179–207.

Molnar, P. & Tapponnier, P., 1975. Cenozoic tectonics of Asia: effects of a continental collision, *Science,* **189**(4201), 419–426.

Molnar, P., England, P. & Martinod, J., 1993. Mantle dynamics, uplift of the Tibetan plateau, and the Indian monsoon, *Rev. Geophysics,* **31**(4), 357–396.

Mooney, W.D., Laske, G. & Masters, G., 1998. Crust 5.1: a global crustal model at 5× 5, *J. geophys. Res.,* **103**(B1), 727–747.

Pasyanos, M.E., Masters, G., Laske, G. & Ma, Z., 2014. Litho1. 0: an updated crust and lithospheric model of the earth, *J. geophys. Res.,* **119**(3), 2153–2173.

Pratt, J.H., 1855. On the attraction of the Himalaya mountains, and of the elevated regions beyond them, upon the plumb-line in India, *Phil. Trans. R. Soc. Lond.,* **145,** 53–100.

Ritsema, J., Deuss, A.A., Van Heijst, H.J. & Woodhouse, J.H., 2011. S40rts: a degree-40 shear-velocity model for the mantle from new Rayleigh wave dispersion, teleseismic traveltime and normal-mode splitting function measurements, *Geophys. J. Int.,* **184**(3), 1223–1236.

Schmalholz, S.M., Medvedev, S., Lechmann, S.M. & Podladchikov, Y., 2014. Relationship between tectonic overpressure, deviatoric stress, driving force, isostasy and gravitational potential energy, *Geophys. J. Int.,* **197**(2), 680–696.

Singh, A., Mercier, J.P., Ravi Kumar, M., Srinagesh, D. & Chadha, R.K., 2014. Continental scale body wave tomography of India: evidence for attrition and preservation of lithospheric roots, *Geochem. Geophys. Geosyst.,* **15**(3), 658–675.

Singh, S. & Ghosh, A., 2019. Surface motions and continental deformation in the Indian plate and the India-Eurasia collision zone, *J. geophys. Res.,* **124,** (11) , 12 141–12 170.

Stamps, D., Flesch, L., Calais, E. & Ghosh, A., 2014. Current kinematics and dynamics of Africa and the east african rift system, *J. geophys. Res.,* **119**(6), 5161–5186.

Steinberger, B. & Holme, R., 2008. Mantle flow models with core-mantle boundary constraints and chemical heterogeneities in the lowermost mantle, *J. geophys. Res.,* **113**(B5), doi:10.1029/2007JB005080.

Wang, X., Holt, W.E. & Ghosh, A., 2015. Joint modeling of lithosphere and mantle dynamics: evaluation of constraints from global tomography models, *J. geophys. Res.,* **120**(12), 8633–8655.

Wang, X., Holt, W.E. & Ghosh, A., 2019. Joint modeling of lithosphere and mantle dynamics: sensitivity to viscosities within the lithosphere, asthenosphere, transition zone, and D" layers, *Phys. Earth planet. Inter.,* **293,** p. 106263, doi:10.1016/j.pepi.2019.05.006.

Zheng, G., Wang, H., Wright, T.J., Lou, Y., Zhang, R., Zhang, W., Shi, C., Huang, J. & Wei, N., 2017. Crustal deformation in the India-Eurasia collision zone from 25 years of GPS measurements, *J. geophys. Res.,* **122**(11), 9290–9312.

SUPPORTING INFORMATION

Supplementary data are available at *GJI* online.

Figure S1 (a) Absolute viscosities (η) used in our lithosphere model (published in Singh & Ghosh 2019) and (b) the viscosity variations within our study region. The area near Shillong plateau has been modified to have viscosities similar to the intraplate regions.
Figure S2 Compensated density (in g cm^{-3}) of lithospheric mantle for (a) CRUST2.0, (b) CRUST1.0 and (c) LITHO1.0 models.
Figure S3 Correlation coefficients between moment tensors from CMT catalogue and deviatoric stress tensors predicted using various models.
Table S1 Summary of results.

Please note: Oxford University Press is not responsible for the content or functionality of any supporting materials supplied by the authors. Any queries (other than missing material) should be directed to the corresponding author for the paper.